Title

Effects of ligand binding on the association properties and conformation in solution of retinoic acid receptors RXR and RAR11Edited by M. F. Moody

Journal

Journal of Molecular Biology, 307(2)

ISSN

0022-2836

Authors

Egea, Pascal F
Rochel, Natacha
Birck, Catherine
et al.

Publication Date

2001-03-01

DOI

10.1006/jmbi.2000.4409

Peer reviewed

doi:10.1006/jmbi.2000.4409 available online at http://www.idealibrary.com on IDEAL® J. Mol. Biol. (2001) 307, 557–576

JMB

Effects of Ligand Binding on the Association Properties and Conformation in Solution of Retinoic Acid Receptors RXR and RAR

Pascal F. Egea[1]†, Natacha Rochel[1]†, Catherine Birck[2] Patrice Vachette[3], Peter A. Timmins[4] and Dino Moras[1]*

[1]*Laboratoire de Biologie et Génomique Structurales Institut de Génétique et Biologie Moléculaire et Cellulaire, CNRS/INSERM/ ULP/Collège de France, Parc d'Innovation BP163 1 rue Laurent Fries, 67404 Illkirch cedex, France*

[2]*Groupe de Cristallographie Biologique, Institut de Pharmacologie et Biologie Structurale, CNRS, 205 Route de Narbonne, 31077 Toulouse France*

[3]*Laboratoire pour l'Utilisation du Rayonnement Electromagnétique, Centre niversitaire Paris-Sud Bâtiment 209d, B.P.34, 91898 Orsay cedex, France*

[4]*Large-Scale Structures Group, Institut Laue-Langevin, avenue des Martyrs B.P. 156 38042 Grenoble cedex 9 France*

In higher eukaryotes, vitamin A derived metabolites such as 9-*cis* and all-*trans* retinoic acid (RA), are involved in the regulation of several essential physiological processes. Their pleiotropic physiological effects are mediated through direct binding to cognate nuclear receptors RXRs and RARs that act as regulated transcription factors belonging to the superfamily of nuclear hormone receptors. Hormone binding to the structurally conserved ligand-binding domain (LBD) of these receptors triggers a conformational change that principally affects the conserved C-terminal transactivation helix H12 involved in transcriptional activation.

We report an extensive biophysical solution study of RARα, RXRα LBDs and their corresponding RXRα/RARα LBD heterodimers combining analytical ultracentrifugation (AUC), small-angle X-ray and neutron scattering (SAXS and SANS) and *ab initio* three-dimensional shape reconstruction at low resolution. We show that the crystal structures of RXRs and RARs LBDs correlate well with the average conformations observed in solution. Furthermore we demonstrate the effects of 9-*cis*RA and all-*trans*RA binding on the association properties and conformations of RXRα and RARα LBDs in solution.

The present study shows that in solution RARα LBD behaves as a monomer in both unliganded and liganded forms. It confirms the existence in solution of a ligand-induced conformational change towards a more compact form of the LBD. It also confirms the stability of the predicted RXRα/RARα LBD heterodimers in solution. SAS measurements performed on three different types of RXRα/RARα LBD heterodimers (*apo/apo*, *apo/holo* and *holo/holo*) with respect to their ligand-binding site occupancy show the existence of three conformational states depending on the progressive binding of RA stereoisomers on RARα and RXRα LBD subunits in the heterodimeric context. These results suggest that the subunits are structurally independent within the heterodimers.

Our study also underlines the particular behaviour of RXRα LBD. In solution unliganded RXRα LBD is observed as two species that are unambiguously identified as homotetramers and homodimers. Molecular modelling combined with SAS data analysis allows us to propose a structural model for this autorepressed *apo*-tetramer. In contrast to the monomeric state observed in the crystal structure, our data show that in solution active *holo*-RXRα LBD bound to 9-*cis*RA is a

†These authors contributed equally to the work.

Abbreviations used: LBD, ligand binding domain; NR, nuclear receptor; 9-*cis*RA, 9-*cis*-retinoic acid, all-*trans*RA, all-*trans* retinoic acid; RXR, retinoid X receptor; RAR, retinoic acid receptor; DBD, DNA-binding domain; SAS, small-angle scattering, SAXS, small-angle X-ray scattering; SANS, small-angle neutron scattering; AUC, analytical ultracentrifugation; AGF, analytical gel filtration; DAM, dummy atom model; PAGE, polyacrylamide gel electrophoresis; Chaps, 3-((3 cholamidopropyl) dimethyl ammonio)-1-propane sulfonate; $C_{12}M$, *n*-Dodecyl α-D-maltoside; DIFP, di-isopropyl fluoro phosphate; DTT, dithiothreitol.

E-mail address of the corresponding author: moras@igbmc.u-strasbg.fr

0022-2836/01/0020557–20 $35.00/0

homodimer regardless of the protein concentration. This study demonstrates the crucial role of ligands in the regulation of homodimeric *versus* heterodimeric association state of RXR in the NR signalling pathways.

Keywords: nuclear receptors; RXR/RAR heterodimers; conformational changes; solution study; small-angle scattering; analytical ultracentrifugation

*Corresponding author

Introduction

Lipophilic hormones including retinoids, steroids, vitamin D_3, thyroxin and eicosanoids are potent regulators of development, cell division and differentiation, organ physiology and metabolism and homeostasis. The pleiotropic effects of these hydrophobic hormones are mediated through specific intracellular proteins belonging to the nuclear receptor (NR) superfamily[1] and whose principal target for action is in the nucleus. All members of this superfamily share a common six functional and structural domain architecture. The C domain (~70-80 amino acids) is highly conserved and responsible for specific DNA binding of the receptor to its target DNA sequence and weak dimerization. The E domain (~250 amino acid residues) namely the ligand binding domain (LBD) is moderately conserved in sequence across members of the family and is responsible for hormone binding and strong dimerization; it carries the ligand-dependent activation function (AF-2) which is critical for the regulation of transcription.

Retinoic acid receptors RARs and RXRs mediate the effects of retinoids, metabolites deriving from vitamin A (retinol). Whereas RARs bind both stereoisomers of retinoic acid: 9-*cis* retinoic acid (9-*cis*RA) and all-*trans* retinoic acid (all-*trans*RA), RXRs bind only the 9-*cis* stereoisomer of retinoic acid.[2,3] Although RXRs can form homodimers, they function as important auxiliary proteins that regulate high affinity DNA-binding and enhance transcriptional activity through heterodimer formation with other members of the superfamily receptors such as RAR, TR (thyroid hormone receptor), VDR (vitamin D_3 receptor), PPAR (peroxisome proliferating activator receptor) and also with orphan receptors.[4,5] The homo and hetero-dimerization complexes of RXR are targeted to the promoters they regulate by DNA sequences known as hormone response elements. The correct dimerization on the DNA is required to recruit the functional set of coactivators or corepressors to the transcription complex. Indeed *in vitro* and *in vivo* studies in mouse have shown that the functional units involved in the transduction of the retinoid signal are RXR/RAR heterodimers.[6,7] It has been shown that in RXR/RAR heterodimers, both subunits are fully competent for ligand binding.[8,9] Nevertheless, in such heterodimers, activation by RXR specific retinoids seems to be subordinated to the presence of an agonist ligand on the RAR subunit.[10]

Several LBD crystal structures of different nuclear receptors have been solved for RXR,[11,12] RAR,[13,14] TR,[15] PPAR,[16] ER,[17] PR[18,19] and VDR.[20] Taken together all the structures confirm the existence of a common fold, the so-called helical sandwich fold for LBDs[21] and show that ligands induce major structural changes upon binding.[22,23] The existence of a conformational change between an «open» *apo*-form and a compact «closed» *holo*-form has been highlighted in the direct comparison between the two X-ray structures of *apo*-RXRα[11] and *holo*-RXRα bound to 9-*cis*RA[12] showing the same receptor in its two extreme conformational states (Figure 1(a) and (b)). Furthermore, the comparison of agonist *versus* antagonist bound LBDs revealed the existence of two very distinct conformations for the C-terminal transactivation helix H12 positioned in two conserved hydrophobic grooves displayed at the NR LBD surface (Figure 1(a) and (c)). These crystallographic studies strongly support the notion of a unique *holo*-agonist conformation among all NR LBDs. Furthermore, the crystal structures of two LBD heterodimers of RXRα/RARα[24] and RXRα/PPARγ[25] revealed that the heterodimeric interface is similar to those observed in the *apo*-RXRα homodimer and *holo*-ERα/β homodimers; this latter point allowed us to generate several heterodimer models in different liganded states (Figure 1(d), (e) and (f)).

X-ray crystallography provides information at the atomic level but does not give direct insight on protein conformation and association state in solution. Here we describe a biophysical study in which we characterize the conformational states of RXRα wild-type (wt) and Phe313Ala mutant (mt) and RARα wild-type LBD single species and their heterodimeric associations (RXRα/RARα) in solution by combining small-angle neutron scattering SANS, small-angle X-ray scattering (SAXS), analytical ultracentrifugation (AUC) and analytical gel filtration (AGF). This study shows the effects of the natural ligands (9-*cis*RA and all-*trans*RA) on receptor conformation and oligomeric association and provides the first direct evidence for a ligand-induced conformational change of NR LBDs in solution. Taking advantage of recent progress in the calculation of scattering patterns from crystallographic structures[26] or models[27] (for a review see

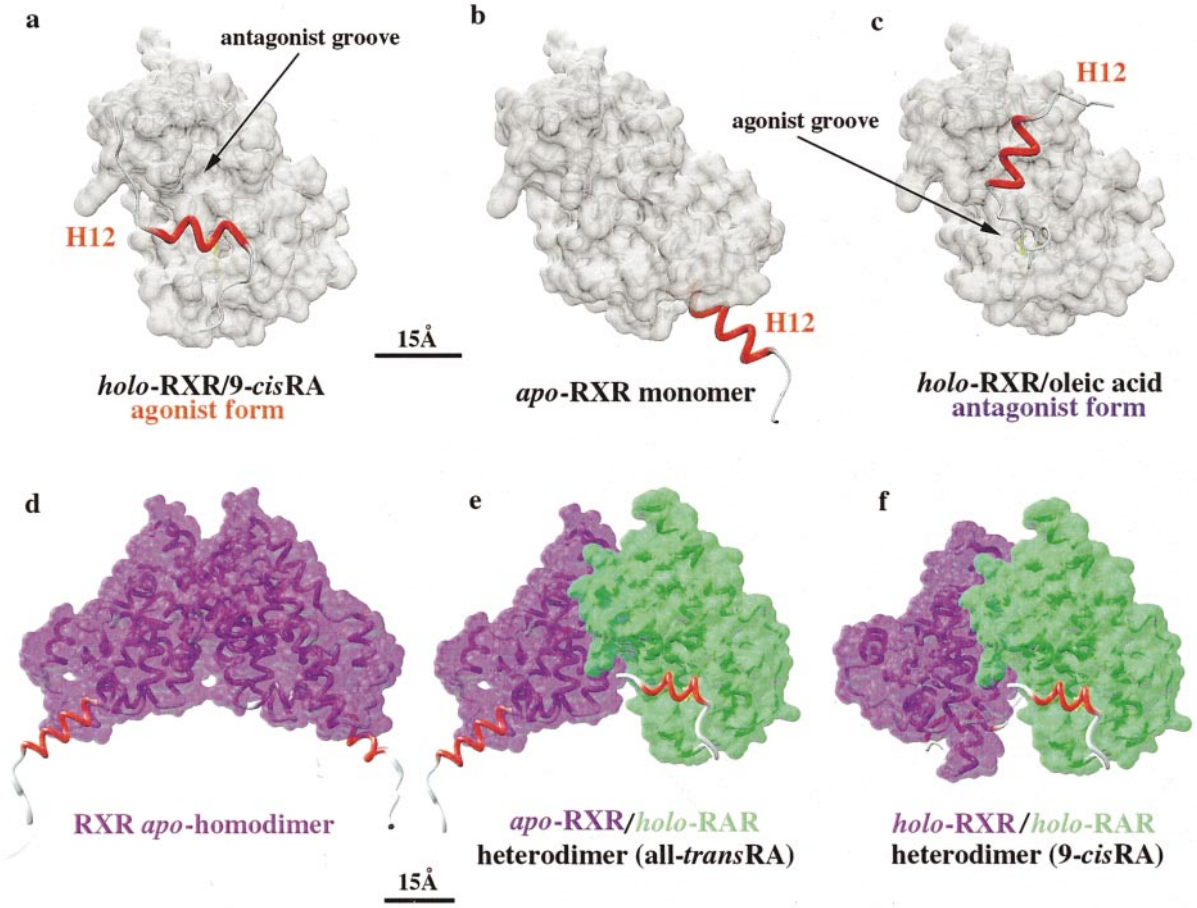

Figure 1. Structural models of RXR and RAR LBDs. Distinct conformations adopted by transactivation helix H12 in liganded RXRα LBDs. (a) Crystallographic structure of agonist *holo*-RXRα LBD (wild-type protein) bound to its natural ligand 9-*cis*RA,[12] the transactivation helix H12 is in agonist conformation and occupies the agonist groove. (b) Crystallographic structure of *apo*-RXRα LBD.[11] The transactivation helix H12 adopts an extended conformation, extended towards the solvent. (c) Crystallographic structure of antagonist *holo*-RXRα LBD (Phe313Ala mutant protein) bound to oleic acid as observed in a heterodimeric structure,[24] the transactivation helix H12 is in antagonist conformation and occupies the antagonist groove. Homo and heterodimeric association modes for RXRα and RARα LBDs. Homodimeric arrangement of *apo*-RXRα[11] and heterodimeric arrangement of RXRα/RARα.[24] RXRα and RARα subunits are depicted in blue and green, respectively. Ligands, respectively, 9-*cis*RA for RXRα and all-*trans*RA for RARα, are depicted in yellow. (d) *Apo*-RXRα homodimer. (e) *Apo*-RXRα/*holo*-RARα heterodimer with all-*trans*RA. (f) *Holo*-RXRα/*holo*-RARα heterodimer with 9-*cis*RA. Solvent-accessible surfaces have been calculated with *MSMS* and are rendered by transparency with *DINO*.[63] Transactivation helix 12, depicted in red, and the loop region between helices H11 and H12 have been omitted from surface calculations. The relative orientations are identical and scale bars are indicated.

Byron & Gilbert),[28] we propose structural models accounting for our experimental data.

Results and Discussion

Analytical gel filtration analysis and homogeneity of solutions of RXRα and RARα ligand binding domains

As a prerequisite for the AUC and SAS investigations, we carried out an AGF study to characterize RXRα, RARα and RXRα/RARα LBD solutions in terms of polydispersity and oligomeric association state of the proteins (Table 1 and Materials and Methods).

The wild-type RARα LBD ($M_r = 27{,}200$ Da) behaves as a monomeric species. All three species of RXRα/RARα heterodimers ($M_r = 55{,}600$ Da) in the three different liganded states *apo/apo*, *apo/holo* (all-*trans*RA in RARα subunit) and *holo/holo* (9-*cis*RA on both RXRα and RARα subunits) could be purified as stable entities with no detectable aggregation or dissociation. The copurification procedure we used allowed us to achieve a proper RXRα *versus* RARα stoichiometry. Wild-type RXRα LBD exhibits a more complex solution behaviour. The wild-type RXRα LBD bound to 9-*cis*RA forms a single stable species with no detectable aggregation or equilibrium. The apparent molecular weight is similar to that determined for RXRα/RARα heterodimers and close to that expected for

Table 1. Analytical gel filtration results

Protein	Ligand	Gel filtration experiments	
		Experimental M_r (Da)	Experimental R_h (Å)
RARα	No ligand	26,600	23.8
RARα	All-*trans*RA	26,600	23.8
wt[a] RXRα	No ligand	99,700	40.7
wt[a] RXRα	No ligand	33,100	26.2
wt[a] RXRα	9-*cis*RA	50,100	31.3
mt[b] RXRα	No ligand	45,700	30.1
mt[b] RXRα	9-*cis*RA	45,700	30.1
RXRα/RARα	No ligand/no ligand	50,100	31.3
RXRα/RARα	No ligand/all-*trans*RA	50,100	31.3
RXRα/RARα	9-*cis*RA/9-*cis*RA	50,100	31.3

[a] wt, wild-type RXRα LBD.
[b] mt, mutant F313A RXRα LBD.

holo-homodimers ($M_r = 56{,}800$ Da). Note that we crystallized the *holo*-RXRα LBD used in this solution study[12] and the crystal structure showed that the basic molecular entity is a monomer. Unliganded RXRα LBD solutions contained two separable species. The high molecular mass species is stable while the other is able to reassociate into the first one. At this stage of the study, the identification of these two species in terms of oligomeric state was delicate, but it was reasonable to suppose the existence of *apo*-homotetramers and *apo*-homodimers of RXRα LBDs. In contrast both the unliganded and liganded mutant RXRα LBD elute as a single stable species of apparent molecular mass similar to those determined for RXRα/RARα heterodimers and *holo*-wtRXRα homodimers.

Both homogeneity and stability of the samples used here have been checked by native PAGE (Figure 2) and confirmed the accuracy of the estimated oligomeric states observed by AGF. The experimental values of hydrodynamic radius obtained for RARα LBD monomeric, RXRα LBD homodimeric and RXRα/RARα LBD heterodimeric species are close to the experimental values of radius of gyration obtained by SAXS and SANS in H_2O buffers (see below).

Analytical ultracentrifugation characterization of shape and oligomer formation

AUC experiments were carried out at protein concentrations ranging from 0.5 to 1.8 mg/ml (Materials and Methods) to characterize the association state of RXRα and RARα LBD species in solution as well as their molecular mass, shape and stability[29-31] (Table 2 and Figure 3).

Equilibrium sedimentation experiments

For RXRα/RARα heterodimers, the molecular mass of $M_r = 54{,}500$ Da (Table 2 and Figure 3(c)) is in excellent agreement with the expected value of 55,600 Da. Least-squares fitting performed on sedimentation equilibrium profiles showed that the best fit was achieved when assuming a purely heterodimeric monodisperse system. Assuming a dissociation equilibrium of heterodimer towards free monomers of RXRα and RARα did not yield any improved fit. This is direct evidence of the extreme stability of RXRα/RARα heterodimers in solution. The same conclusions were derived from similar experiments carried out on *holo*-RXRα LBDs of both wild-type and mutant receptor that gave molecular mass values of 55,400 Da and 56,200 Da, respectively (Table 2 and Figure 3(b)).

Table 2. Analytical ultracentrifugation results

Protein	Ligand	Sedimentation velocity		Sedimentation equilibrium experimental M_r (Da)
		Experimental S	Calculated S	
RXRα/RARα	9-*cis*RA/9-*cis*RA	3.9 S/(3.9 S)[c]	3.9 S (heterodimer)	54,500 ± 550
wt[a] RXRα	No ligand	5.4 S/(5.7 S)	6.1 S (homotetramer)	108,000 ± 2500
wt[a] RXRα	9-*cis*RA	3.7 S/(3.9 S)[c]	3.9 S (homodimer)	56,200 ± 1000
mt[b] RXRα	9-*cis*RA	-	3.9 S (homodimer)	55,400 ± 620
RARα	All-*trans*RA	2.8 S/(2.8 S)[c]	2.7 S (monomer)	-

Sedimentation coefficient s units are expressed in Svedberg units (S). Calculated sedimentation coefficients were computed with *AtoB* and *HYDRO* using crystallographic structures (see Materials and Methods) and assuming the oligomeric state indicated between parenthesis.
[a] wt refers to wild-type RXRα LBD.
[b] mt, mutant F313A RXRα LBD.
[c] Values between parenthesis were determined from $g(S^*)$ analysis, whereas other values were determined from midpoint and second point analyses (see Materials and Methods).

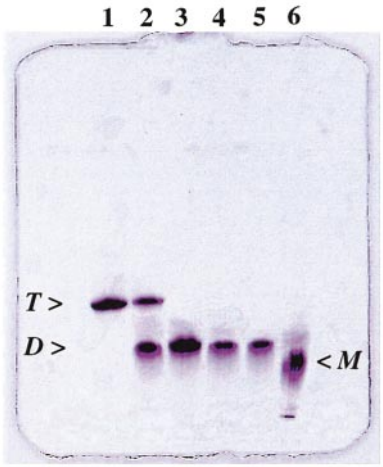

Figure 2. Native polyacrylamide gel (gradient 8-25 %) showing the homogeneity of protein solutions used in this biophysical study by SAS and AUC. Lane 1, *apo*-RXRα tetramer; lane 2, *apo*-RXRα dimer and tetramer; lane 3, mutant *apo*-RXRα; lane 4, *holo*-RXRα/9-*cis*RA; lane 5, *holo*-RARα/all-*trans*RA; lane 6, *holo*/*holo*-RXRα/RARα/9-*cis*RA heterodimer. *T*, *D* and *M* indicate tetrameric, dimeric (homo- and hetero-) and monomeric LBD species, respectively.

In the case of wild-type *apo*-RXRα LBD, only the stable high molecular mass fraction was investigated. The molecular mass of 108,000 Da derived from data analysis corresponds to an *apo*-homotetramer (Table 2 and Figure 3(a)). Allowing for a dimer/tetramer equilibrium only yielded a marginal improvement of the fit while no monomer of RXRα LBD was detected. This result confirms the extreme stability of the *apo*-tetrameric form of RXRα LBD. Previous studies performed on solutions of RXRα LBDs, mainly by measuring the decay of fluorescence anisotropy,[32-34] lead to equilibrium dissociation constants of 155 nM and 4.4 nM for the formation of RXRα dimers from monomers and of tetramers from dimers, respectively.

Sedimentation velocity measurements

The apparent sedimentation coefficients of several RXRα and RARα LBD species determined from solutions which had previously been shown to be monodisperse both by gel filtration and equilibrium sedimentation experiments were compared to those calculated using their respective crystal structures. Experimental coefficients were determined by three distinct analytical methods (Materials and Methods) that all yielded similar values. The experimental and calculated values essentially show a good agreement (Table 2).

The monomeric RARα LBD exhibits an experimental sedimentation coefficient of $s = 2.8$ S, close to the structure based value (Figure 3(d)). For *holo*-RXRα LBDs and RXRα/RARα LBD heterodimers, the experimental values ($s = 3.7$ to 4.2 S) are in good agreement with those calculated assuming dimers in both cases (Figure 3(e) and (f)). Thus, in a first approximation, the solution behaviour of LBDs could be correlated to the available crystal structures. In the case of the *apo*-RXRα tetrameric form, the experimental values ($s = 5.4$ to 5.7 S) were compared to those calculated from a model based on SAS results (see below).

An important parameter is the use of dilute solutions for both types of AUC experiments (ranging from 5 to 70 μM), especially in the case of RARα (experiments carried out at 70 μM) and *holo*-RXRα (experiments carried out at 15 to 20 μM). Under such conditions, the observed homodimeric species of *holo*-RXRα cannot be attributed to concentration effects, interaction between particles and therefore non-ideality of the solution. Indeed our AUC results show unambiguously the homodimeric nature of RXRα LBD bound to 9-*cis*RA, its natural ligand.

Small angle scattering study by SAXS and SANS

Whereas RAR binds both 9-*cis* and all-*trans* stereoisomers of retinoic acid, RXR only binds the 9-*cis* stereoisomer. Solutions of RARα and RXRα LBDs, either unliganded or in specific combination with their ligands, were studied by SAXS and SANS. No aggregation was detected and all solutions appear to be monodisperse with Guinier plots linear over an appropriate angular range (typically $0.3\text{-}0.5 < QR_G < 1.2\text{-}1.8$ according to each specific case). The values of the radius of gyration of the different species are presented in Table 3, together with the estimate of the molecular mass derived from the value of the intensity at the origin which is also in agreement with the value predicted from the amino-acid sequence (Materials and Methods). A selection of four Guinier plots is presented in Figure 4. The distance distribution function $P(r)$ was also calculated from each scattering pattern allowing the determination of the maximal diameter D_{max} and of the radius of gyration (Materials and Methods). Six such representative curves are shown in Figure 5 while the values of D_{max} and of the radius of gyration derived from $P(r)$ determination are given in Table 3 for each LBD species. Calculated scattering curves from crystallographic or modelled structures were also fitted to our experimental curves, four representative fits are shown in Figure 6.

From the values reported in Table 3, there is a good agreement between experimental values of the radius of gyration obtained from SANS in H_2O buffers and from SAXS. However, significant differences are observed between the experimental values for the radius of gyration obtained from SANS in H_2O or ^2H_2O buffers. This can, in part be explained by the theory of Stuhrmann[35] which predicts a lower radius of gyration for proteins in

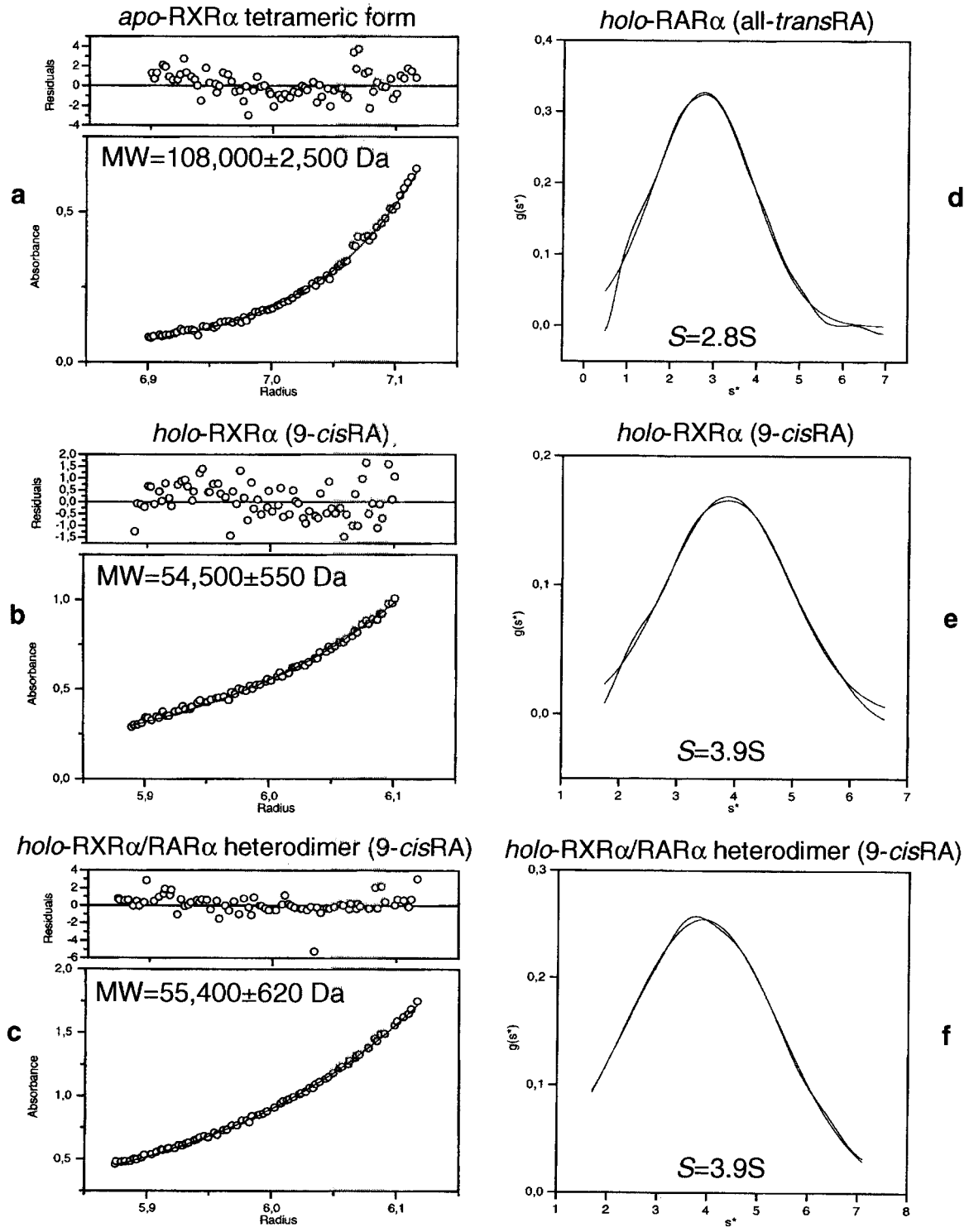

Figure 3. Analytical ultracentrifugation results. Equilibrium sedimentation data results obtained for *apo*-RXRα (a), *holo*-RXRα in presence of 9-*cis*RA (b) and *holo*-RXRα/RARα heterodimers in presence of 9-*cis*RA (c). Concentration radial distributions along with the fitted curves are plotted with their corresponding reduced residual deviations (weighted fit). In all cases experimental curves were fitted assuming a single species system. Experimental molecular masses are indicated. Sedimentation velocity data results obtained for *holo*-RARα in presence of all-*trans*RA (d), *holo*-RXRα in presence of 9-*cis*RA (e) and *holo*-RXRα/RARα heterodimer (f). Data are presented in $g(S^*)$ format using the time-derivative method approach. In each case, the experimental $g(S^*)$ distributions were fitted assuming a single species system. Experimental sedimentation coefficient values s are indicated.

Table 3. SAS results

A. *SAS results (from Guinier analysis)*

Protein	Ligand	R_G Neutron (Guinier) (Å) 100% ^2H_2O buffer	R_G Neutron (Guinier) (Å) 100% H_2O buffer	R_G X-rays (Guinier) (Å)	Molecular mass M_r from $I(0)$ (Da)
RARα	No ligand	18.0 ± 0.2	22.2 ± 0.3	22.3 ± 0.3	27,000 ± 3000
RARα	All-*trans*RA	17.2 ± 0.2	21.4 ± 0.3	-	-
RXRα/RARα	No ligand/no ligand	23.2 ± 0.2	26.8 ± 0.3	26.3 ± 0.3	-
RXRα/RARα	No ligand/all-*trans*RA	22.4 ± 0.2	25.7 ± 0.3	25.5 ± 0.3	52,500 ± 5000
RXRα/RARα	9-*cis*RA/9-*cis*RA	21.7 ± 0.2	25.0 ± 0.3	26.0 ± 0.3	-
wt[a] RXRα[c]	No ligand	29.2 ± 0.2	32.1 ± 0.3	32.8 ± 0.3	99,000±5000
wt[a]RXRα[d]	No ligand	25.2 ± 0.2	28.1 ± 0.3	28.0 ± 0.3	-
wt[a] RXRα	9-*cis*RA	23.9 ± 0.2	27.1 ± 0.3	26.7 ± 0.3	48,000 ± 5000
mt[b] RXRα	No ligand	25.4 ± 0.2	27.0 ± 0.3	28.5 ± 0.3	51,000 ± 5000
mt[b] RXRα	9-*cis*RA	25.0 ± 0.2	26.8 ± 0.3	28.1 ± 0.3	-

B. *SAS results (from the distance distribution function* P(r))

Protein	Ligand	$P(r)$ Neutron analysis (*ITP* and *GNOM*) in ^2H_2O R_G (Å)	$P(r)$ Neutron analysis (*ITP* and *GNOM*) in ^2H_2O D_{max} (Å)	$P(r)$ X-rays analysis (*GNOM*) (Å) R_G	$P(r)$ X-rays analysis (*GNOM*) (Å) D_{max}
RARα	No ligand	19.5 ± 0.3	67 ± 3	-	-
RARα	All-*trans*RA	18.6 ± 0.3	60 ± 3	-	-
RXRα/RARα	No ligand/no ligand	24.0 ± 0.3	87 ± 3	26.3 ± 0.3	92±3
RXRα/RARα	No ligand/all-*trans*RA	23.2 ± 0.3	79 ± 3	25.5 ± 0.3	85 ± 3
RXRα/RARα	9-*cis*RA/9-*cis*RA	22.4 ± 0.3	71 ± 3	26.0 ± 0.3	80 ± 3
wt[a] RXRα[c]	No ligand	29.4 ± 0.3	92 ± 3	32.6 ± 0.3	95±3
wt[a]RXRα[d]	No ligand	-	-	27.9 ± 0.3	92±3
wt[a] RXRα	9-*cis*RA	23.9 ± 0.3	75 ± 3	-	-
mt[b] RXRα	No ligand	25.4 ± 0.3	85 ± 3	-	-
mt[b] RXRα	9-*cis*RA	24.9 ± 0.3	73 ± 3	-	-

RAR concentrations range from 3 to 5 mg/ml. RXR/RAR concentrations range from 2 to 5 mg/ml. RXR concentrations range from 2 to 10 mg/ml.

[a] wt, wild-type RXRα LBD.

[b] mt, mutant F313A RXRα LBD.

[c] *Apo*-tetrameric form of wild-type RXRα LBD.

[d] *Apo*-dimeric form of wild-type RXRα LBD.

^2H_2O than in H_2O. This is due to the fact that hydrophobic amino acids, which are found predominantly at low radius, have the highest contrast in ^2H_2O, whereas hydrophilic amino acids which are found at high radius have the highest contrast in H_2O. It has also been shown by Svergun *et al*.[36] that in order to fit the extended scattering curve of a number of proteins such as lysozyme or thioredoxin reductase it is necessary to consider the presence of a hydration shell of density somewhat greater than that of bulk water. In the case of ^2H_2O this shell will have a contrast opposite to that of the protein thus reducing the radius of gyration compared with the non-hydrated protein. The effect in H_2O is much smaller as the scattering length density of the water is very close to zero. Therefore it appears that the hydration model inferred in *CRYSON* and *CRYSOL* with a hydration shell of average density of 10-15 % larger than that of the bulk solvent is in agreement with our experimental data and allows us to explain these differences. The values of the radius of gyration obtained from $P(r)$ region analyses are similar to those obtained from small-angle (Guinier) analyses.

Retinoic acid binding induces a conformational change of RARα towards a more compact form

According to the SAS data, upon retinoic acid binding (all-*trans*RA) the RARα LBD undergoes conformational changes from a relaxed *apo*-form to a more compact *holo*-form. The radius of gyration of the *apo*-RAR LBD form is about 0.8 to 1.2 Å larger than that of the *holo*-RAR LBD form, both in deuterated and non-deuterated buffers, a significant difference (Table 3 and Figure 4(a)). For a spherical object with similar R_G, the 0.8 Å decrease in the radius of gyration corresponds to an average 13 % decrease in global volume. As the crystal structures of RXRα ligand binding domain in both its *apo*- and *holo* forms have been solved,[11,12] we used them to perform volume calculations on the same LBD under these two conformational states and found that the decrease in volume was about 10 %, in good agreement with the solution values.

Scattering patterns calculated from crystallographic coordinates were fitted against SANS experimental curves. For *apo* and *holo*-RARα, the curves calculated using the model of *apo*-RXRα yield acceptable fits, thereby suggesting that in

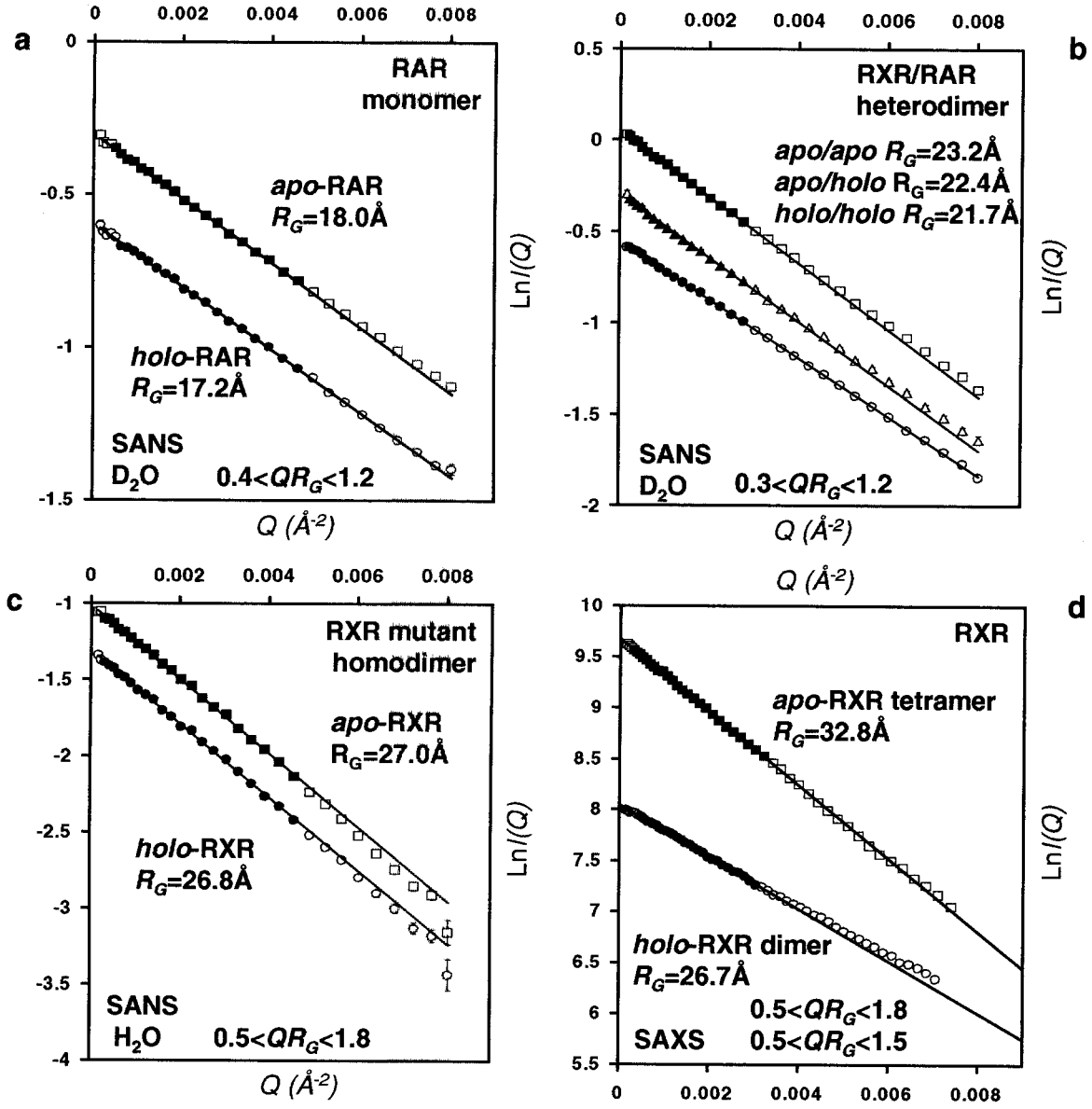

Figure 4. Small angle analysis of SAS data. Guinier plots. (a) Guinier analysis results obtained by SANS in 100 % ^2H_2O buffer for *apo* (squares) and *holo* (circles) RARα LBD. Experimental errors bars are shown. (b) Guinier analysis results obtained by SANS in 100 % ^2H_2O for *apo/apo* (squares) and *apo/holo* (triangles) and *holo/holo* (circles) RXRα/RARα LBD heterodimers. Experimental error bars are shown. (c) Guinier analysis results obtained by SANS in 100 % H_2O buffer for *apo* (squares) and *holo* (circles) mutant RXRα LBD. Experimental error bars are shown. (d) Guinier analysis results obtained by SAXS for *apo* (squares) and *holo* (circles) wild-type RXRα LBD. *apo* wild-type RXRα LBD represents the tetrameric form. Experimental error bars are shown. In all cases effective $Q \cdot R_G$ ranges are indicated. Filled symbols show the experimental points used to determine the R_G values.

solution the monomeric conformation adopted by RARα LBD is close to that observed in the crystalline structure (Figure 6(a)).

$P(r)$ functions were calculated from the experimental SANS and calculated scattering patterns for both species of RARα LBD; the $P(r)$ curve of *apo*-RARα is shown in Figure 5(a). The agreement between the calculated and experimental $P(r)$ curves is acceptable; however, the slight discrepancy observed in the range of long interatomic vectors might be due to the presence of some oligomers in solution. Experimental D_{max} comparison from SANS data obtained for *apo* and *holo*-RARα LBD shows a 7 Å decrease, confirming the effective compaction of LBD upon ligand binding. The R_G values recalculated from $P(r)$ functions are slightly higher than those obtained from the Guinier plots but the R_G difference between unliganded and liganded RARα LBD is conserved (Table 3). Observation of the crystal structures of *apo* and *holo* RXRα LBD monomers shows that ligand binding induces C-terminal helix 12 packing against the

core domain (Figure 1). The general shape of the core is not spherical but rather elongated with its longest axis being roughly colinear to a N to C-terminal axis that will include helix 12 in its more extended position as observed in the *apo*-RXRα crystal structure. D_{max} changes therefore directly reflect the position change of helix 12 upon ligand binding. Although, in solution, helix H12 is likely to adopt a wide range of positions around the particular one observed in the crystal structure of *apo*-RXRα, the experimentally observed average conformation does appear to be more elongated than its *holo* counterpart. Solution studies carried out on PPARγ using NMR spectroscopy[37] confirmed this hypothesis. Interestingly *holo*-RARα LBD has been crystallized bound to several agonist or antagonist compounds but never under its *apo*-form; this latter point probably reflects the high conformational flexibility of the H12 region of the LBD that, combined to a relative hydrophobicity, precludes its crystallization.

Effect of specific ligand binding on RXRα/RARα heterodimer conformation

As already mentioned, RAR binds both 9-*cis* and all-*trans* stereoisomers of retinoic acid whereas RXR only binds the 9-*cis* stereoisomer; in the case of RXR the dissociation constant is $K_D^{9cis} = 1.5$ nM and for RAR the dissociation constants for 9-*cis* and all-*trans* isomers are, respectively, $K_D^{9cis} = 0.8$ nM and $K_D^{\text{all-}trans} = 0.2$ nM.[38,39] Extensive biochemical data have been published on the ligand binding properties of each RXR and RAR subunit within the heterodimer.[40,41] Since retinoids bind with high affinity on their cognate receptors, we investigated the effects of all-*trans*RA and 9-*cis*RA specific and selective binding on RXRα/RARα LBD heterodimers. The decrease in the R_G value upon ligand binding reflects the increase of compactness of RXRα/RARα LBD heterodimers in solution. The unliganded (*apo/apo*) heterodimer is less compact than the half-liganded (*apo/holo*) or its fully liganded counterpart (*holo/holo*). The total R_G decrease from unliganded to fully liganded state amounts to 1.5-1.8 Å for SANS data and 0.8 Å for SAXS data (Table 3 and Figure 4(b)).

Experimental RXRα/RARα scattering curves obtained from both SAXS and SANS measurements were fitted against theoretical curves calculated using crystallographic structures. The models were built using RXRα and RARα monomer crystal structures and assuming the same dimerization interfaces as those observed in the RXRα LBD homodimer and in a RXRα/RARα LBD heterodimer (Figure 1). The experimental intensities obtained with all three heterodimeric complexes are well fitted (Figure 6(b)).

$P(r)$ functions were calculated for all three species of RXRα/RARα LBD heterodimers from the experimental and calculated scattering patterns. The resulting curves are shown for SANS data in Figure 5(d)-(f). The SAXS results are essentially identical. The general trend towards compaction upon ligand binding is found again when comparing D_{max} values with a global decrease of 12-16 Å. It is also visible in the general shape of the $P(r)$, which are superimposable up to around 50 Å, beyond which they show differences according to the liganded state. The agreement between the calculated and experimental $P(r)$ curves is best for the *apo/holo* heterodimer. In the case of the *apo/apo* heterodimer, the two curves are very similar, although the $P(r)$ value of the crystallographic model shows slightly higher values on the large distance side. This might be due to the already mentioned flexibility of the H12 helix in solution which might lead to a decrease of the number of largest distances, while in the crystal model the helices display their maximal extension. The slight discrepancy observed on the *holo/holo* heterodimer is consistently visible on SANS and SAXS data alike. It might be due to some minor association in solution, although the scattering pattern in the small-angle region shows no trace of it. Alternatively, it could be associated with the mobile region of RXRα LBD around helix H2, located at the protein surface on the left-hand side of the RXRα LBD in Figure 1(a), which is poorly defined in the crystal electron density map.[12] Movements of this region might increase somewhat the contribution to the long vector side of the $P(r)$ distribution as compared to that derived from the crystal structure. Whatever the reason for this minor discrepancy, by and large, these results support the conclusion that in solution the subunit arrangement and global conformation within RXRα/RARα LBD heterodimers are close to those observed in the crystalline structures. Besides, our study supports the view that, within an RXRα/RARα LBD heterodimer, each subunit is capable of structurally independent ligand binding and is able to undergo the associated conformational change with an increased compactness of heterodimerically associated LBDs upon ligand binding.

In solution RXRα bound to 9-*cis* retinoic acid, its natural ligand, is a homodimer

The *apo* and *holo* form of mutant RXRα LBD as well as the *holo*-RXRα LBD displayed characteristics consistent with a stable dimer in agreement with gel filtration, analytical ultracentrifugation and native PAGE observations whatever the concentration; no tetrameric species was observed. The R_G values determined by both SANS and SAXS and the molecular mass calculations derived from $I(0)$ determination are close to those observed for heterodimers, thus indicating that the mutant RXRα LBD is essentially a dimeric species in solution regardless of the ligand (Table 3 and Figure 4(c)). This observation was made both in H_2O and ^2H_2O buffers for different protein preparations.

The absence of any detectable equilibrium for both *apo* and *holo* forms of mtRXRα and for

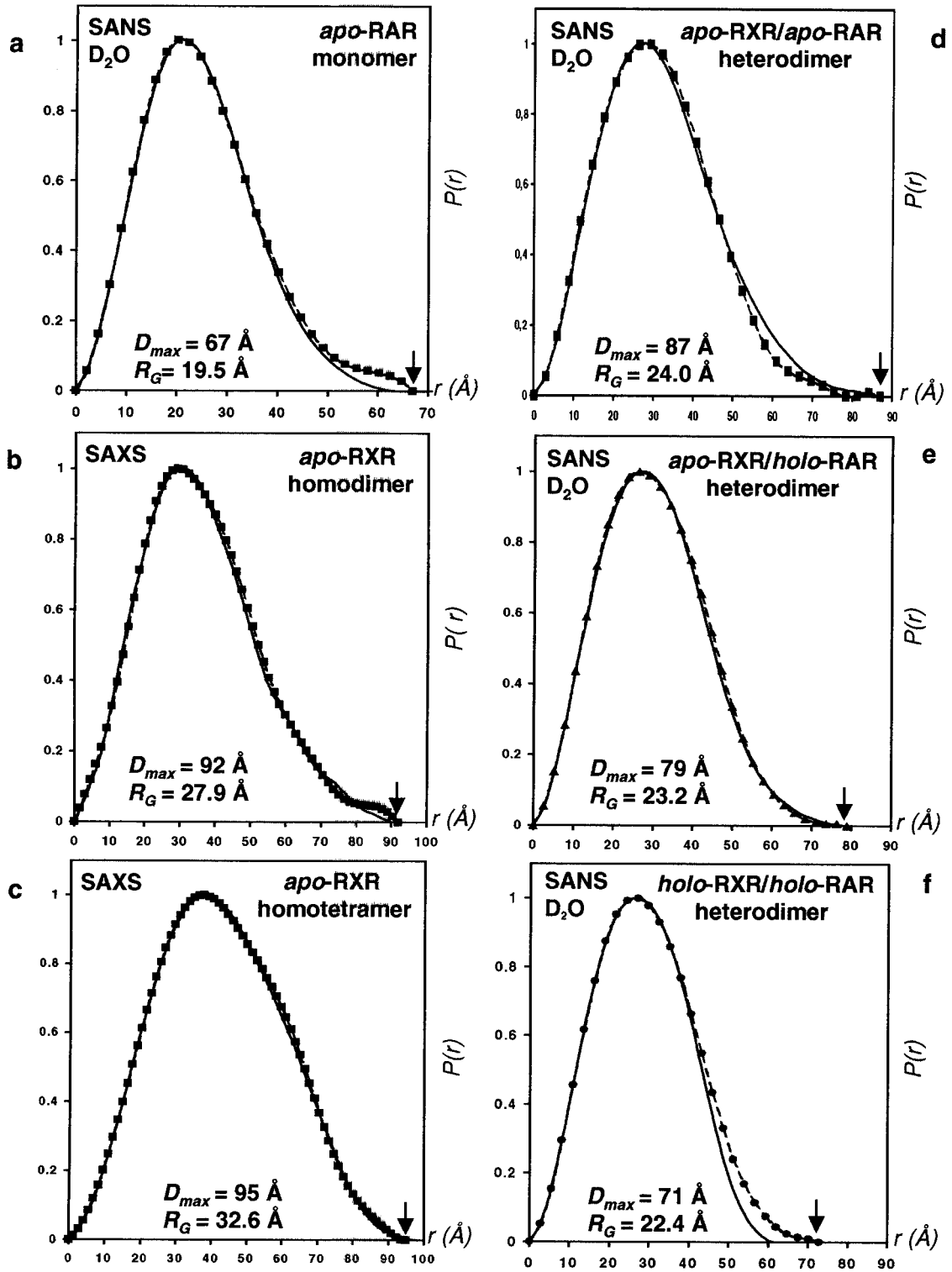

Figure 5 (*legend opposite*)

wild-type *holo*-RXRα LBD allowed us to confidently consider monodisperse solutions with only one RXRα LBD species in all cases. Scattering curve fitting was therefore performed on mutant and wild-type from both SAXS and SANS measurements. The experimental curves were fitted using calculated curves computed assuming homodimer models (Figure 6(c)). The experimental $P(r)$ function estimated from SAXS data of *apo*-RXRα LBD is similar to that calculated using the homodimeric structure of *apo*-RXRα LBD (Figure 5(c) and Table 3).

As already mentioned, the crystal structure of liganded RXRα shows a monomeric species. The discrepancy between the oligomeric state observed in solution and in the crystal might be due to the crystallization conditions of *holo*-RXRα.[12] The mother liquor used for crystallization contained sodium formate (up to 2 M) and viscous alcohols such as glycerol (up to 10 %) and propane 1,2 diol (up to 20 %). AUC experiments carried out in sodium formate (data not shown) show that this salt does not promote the destabilization of *holo*-RXRα homodimers. Such dissociation might be due to viscous alcohols, in particular propane diol. Indeed, in the case of the PPARγ LBD crystallized as a monomer form, it was observed that propane diol induced homodimer dissociation into monomers. Altogether, the AUC and SAS data clearly point to the homodimeric state of *holo*-RXRα LBD in solution.

Apo-RXRα forms stable homo-tetramers in solution

The existence of tetramers for unliganded RXR LBDs has been reported[42-44] but their biological significance remains a matter of controversy although it was proposed that such tetramers could represent a storage form of RXR in the cell. An interesting, although artefactual, tetrameric association mode has been described in the case of a crystal structure of ERα LBD.[19] In such a model, tetrameric association resulted from an intertwining of two canonical homodimers with an intermolecular exchange of helix H12, each helix occupying the antagonist groove of an oppositely positioned LBD. Two crystal structures of *apo*-RXRα LBD have been reported: one corresponding to a dimer[11] and more recently, after this study was completed, a second corresponding to a tetramer.[45]

Having recorded the SAXS profile for the RXRα LBD tetramer a systematic fitting procedure (for a review see Perkins *et al.*)[46] was carried out with modelled tetramers using a model based on *apo*-RXRα LBD homodimer structure. The building block used in modelling was the homodimer with helices 12 occupying the antagonist grooves; the connection between helices H10 and H12 encompassing the helix H11 and the H11-H12 loop was omitted (12 amino acid residues). Two such homodimers were intertwined in a head-to-tail arrangement with their 2-fold symmetry axes exactly superimposed (Figure 7(a)). The distance between the centres of mass and the relative angle between the two dimers were then systematically incremented. The scattering curves from the resulting models were computed with *CRYSOL* and used to fit the experimental SAXS data. The associated χ^2 values are displayed as a function of both fitting parameters in Figure 7(b). The paraboloïdal shape of the surface indicates the existence of a unique solution corresponding to a translation distance of $\tau = 41.5$ Å and a rotation angle of $\kappa = 120°$ (Figure 7(b)). The resulting scattering curve (Figure 6(d)) and distance distribution function (Figure 5(c)) fits to the experimental curves are quite remarkable with identical radii of gyration obtained by both Guinier and $P(r)$ analyses; similar results were obtained from SANS data (Table 3 and Figure 4(d)). The resulting best fit model does not display any steric clash between protein monomers; furthermore the distance separating H10 and H12 C and N termini, respectively, from oppositely arranged monomers belonging to two distinct dimers permitted an easy reconstruction of the missing connection. The modelled tetramer shows an overall elongated, flat and disk-like shape and displays a relative asymmetry. The sedimentation coefficient calculated with *AtoB* and *HYDRO* for this modelled tetramer ($s = 6.1$ S) is fairly close to that obtained experimentally ($s = 5.4$ to 5.7 S) in the AUC experiments (Table 2).

Our solution model for the tetramer is similar to the crystal structure that was reported after completion of this study. In our case, the extended helices H12 from each dimer span across and occupy the coactivator binding sites of the adjacent dimer. In such a configuration, this physically precludes the binding of coactivators to RXR; such model therefore supports the auto-repression mechanisms involving the AF2 region helix that has been proposed.[47] The tetramerization interface mediated by the exchange of the four helices H12 (Figure 7(c)) explains the remarkable stability and

Figure 5. High angle analysis of SAS data. $P(r)$ distance distribution functions. (a) Distance distribution function $P(r)$ for *apo*-RARα. The curve calculated from experimental SANS data (squares) is displayed with error bars and curve calculated from monomeric RARα LBD crystallographic structure is displayed as a continuous line. (b) Distance distribution function $P(r)$ calculated from the SAXS data of wild-type *apo*-RXRα LBD dimer. The curve calculated from experimental SAXS data (circles) is displayed with error bars and curve calculated from the RXRα LBD homodimer crystallographic structure is displayed as a continuous line. (c) Distance distribution function $P(r)$ calculated from the SAXS data of wild-type *apo*-RXRα LBD tetramer. The curve calculated from experimental SAXS data (squares) is displayed with error bars and curve calculated from the modelled *apo*-RXRα LBD tetramer is displayed as a continuous line. (d), (e) and (f) Distance distribution functions $P(r)$ for *apo/apo* (squares), *apo/holo* (bound to all-*trans*RA) (triangles), and *holo/holo*- (bound to 9-*cis*RA) (circles) RXRα/RARα LBD heterodimers. Curves calculated from experimental SANS data are displayed with error bars and curves calculated from the RXRα/RARα LBD heterodimer crystallographic structures are displayed as continuous lines. In all cases distance distribution $P(r)$ functions were computed with *GNOM* and *CRYSON/CRYSOL*. The arrows stand for the estimated values of D_{max} and the values of the radius of gyration obtained from $P(r)$ analysis are indicated.

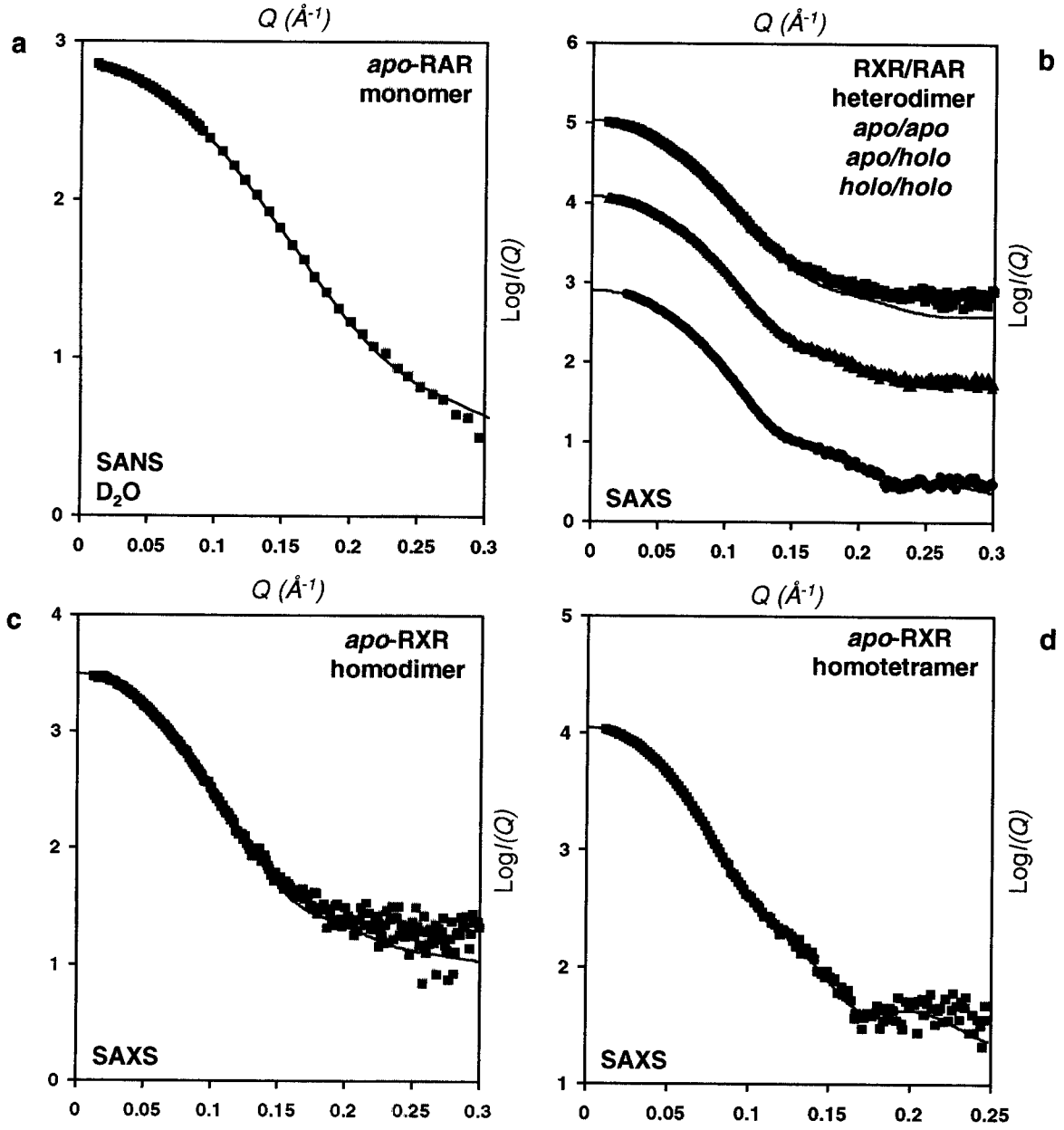

Figure 6. Scattering curves $I(Q)$ fits. (a) SANS scattering curve fitting for *apo*-RARα LBD. The experimental scattering curve (squares) was fitted using *CRYSON* against the calculated curve shown (continuous line) based on the crystallographic structure of monomeric RARα LBD. (b) SAXS scattering curves fitting for RXRα/RARα heterodimers. The experimental scattering curves corresponding to *apo/apo* (squares), *apo/holo* (bound to all-*trans*RA) (triangles) and *holo/holo*- (bound to 9-*cis*RA) (circles) RXRα/RARα heterodimers were fitted using *CRYSOL* calculated curves (continuous lines) based on the crystallographic structure of RXRα/RARα LBD heterodimer. (c) SAXS scattering curves fitting for wild-type *apo*-RXRα LBD dimer. The experimental scattering curve (circles) was fitted using *CRYSOL* against the calculated curve (continuous line) based on crystallographic structures of RXRα LBD homodimer. (d) SAXS scattering curves fitting for wild-type *apo*-RXRα LBD tetramer. The experimental scattering curve (squares) was fitted using *CRYSOL* against the calculated curve (continuous lines) based on the modelled *apo*-RXRα LBD tetramer.

the slow spontaneous dissociation of this compact tetrameric arrangement of RXRα. Indeed, this model also demonstrates the role of helix H11 in the formation and stability of the tetramer. A similar model for *apo*-tetrameric arrangement has already been proposed,[42,43] but it was not based on structural experimental data but only on virtual docking of two *apo*-RXRα homodimers. This model used mutational data affecting the three phenylalanine residues Phe436, Phe437 and Phe439 on helix H11 of RXRα. This study showed that mutations in Phe438 and Phe439 completely abol-

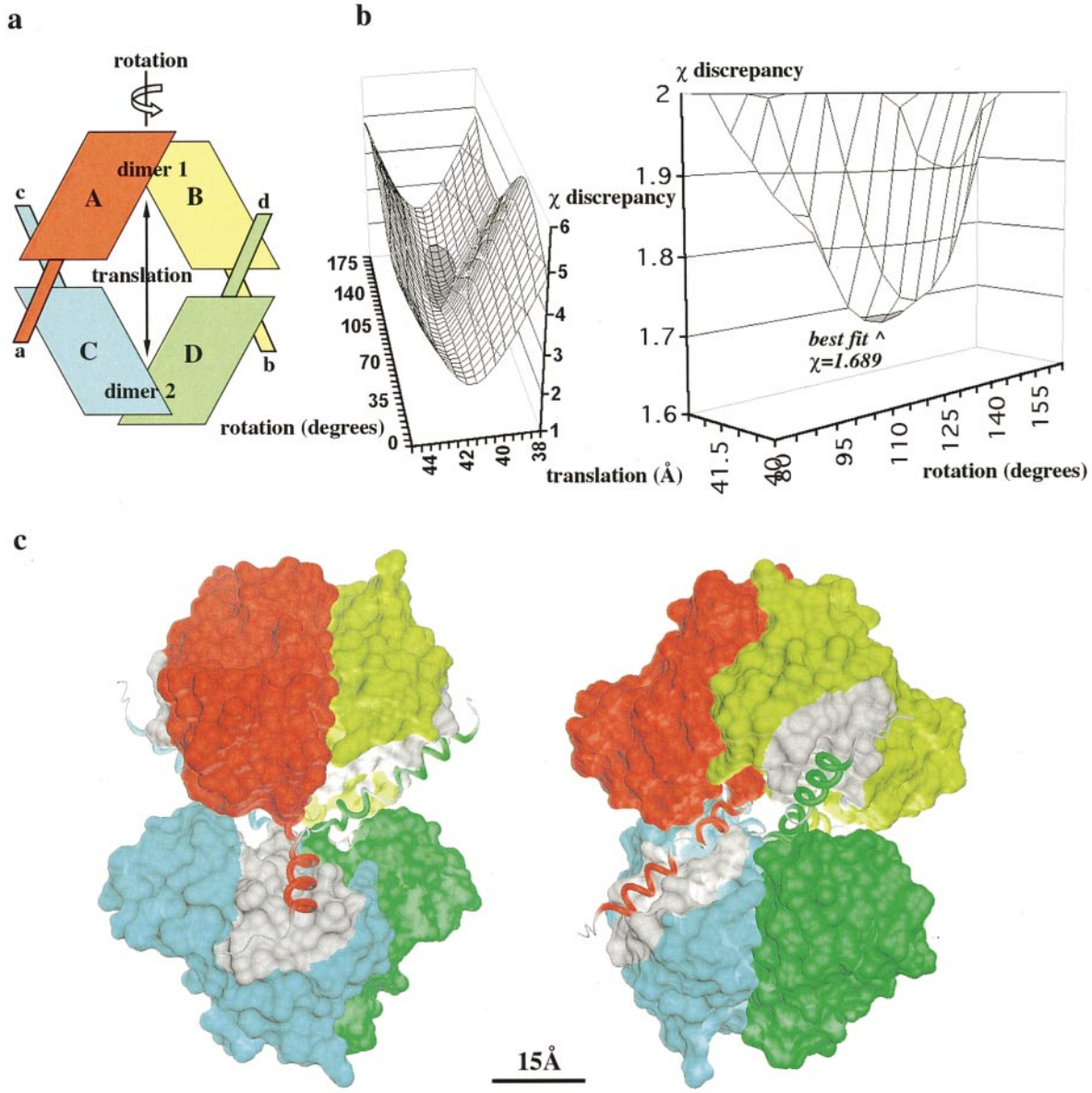

Figure 7. Modelling of *apo*-RXRα LBD tetramer using SAXS data. (a) Schematic model of *apo*-RXRα tetrameric arrangement used for the systematic fitting procedure in *CRYSOL*. Each RXRα monomer is modelled as a core domain (labelled A, B, C and D) and its corresponding transactivation helix H12 (labeled a, b, c, and d) in an extended conformation allowing intertwining of two homodimers to form a homotetramer. (b) Discrepancy χ between the experimental SAXS data and the scattering from tetrameric models as a function of both the translational distance and the rotational orientation between the two dimers constituting the *apo*-tetramer model as depicted in (a). A general view of the total conformational space explored as well as a close-up view of the single minimum region is displayed. Best-fit model corresponds to a discrepancy of $\chi = 1.687$ and is obtained for $\kappa = 120^\circ$ and $\tau = 41.5$ Å (respectively the relative rotation around the 2-fold symmetry axis and the distance between the centers of mass of the two dimers). Intensities and fits were computed with *CRYSOL* with angular and translational increments of 5° and 0.5 Å, respectively. (c) Structure of the best-fit modelled *apo*-RXRα LBD tetramer. The tetramer surface is drawn with the same colour code as used in (a). The helices H11 and H12 involved in tetramerization have been pointed out. The interaction surfaces beetween helices H12 and the LBD-cores are coloured in white, they correspond to the hydrophobic antagonist grooves. A scale bar is indicated.

ished the ability of RXRα to self-associate into tetramers but did not affect homodimer formation or DNA-binding functions. These hydrophobic residues are in close van der Waals contact and concentrated in the central region of the tetramer at the dimer/dimer interface. The comparison of *apo* and *holo*-RXRα LBD crystal structures[12,23] showed the role of helix H11 hydrophobic residues (in particular Phe437, Phe438 and Phe439) in the solvating and desolvating processes in the *apo* to *holo* transition. In particular, in the *apo*-form, the Phe439 residue is exposed to the solvent and therefore

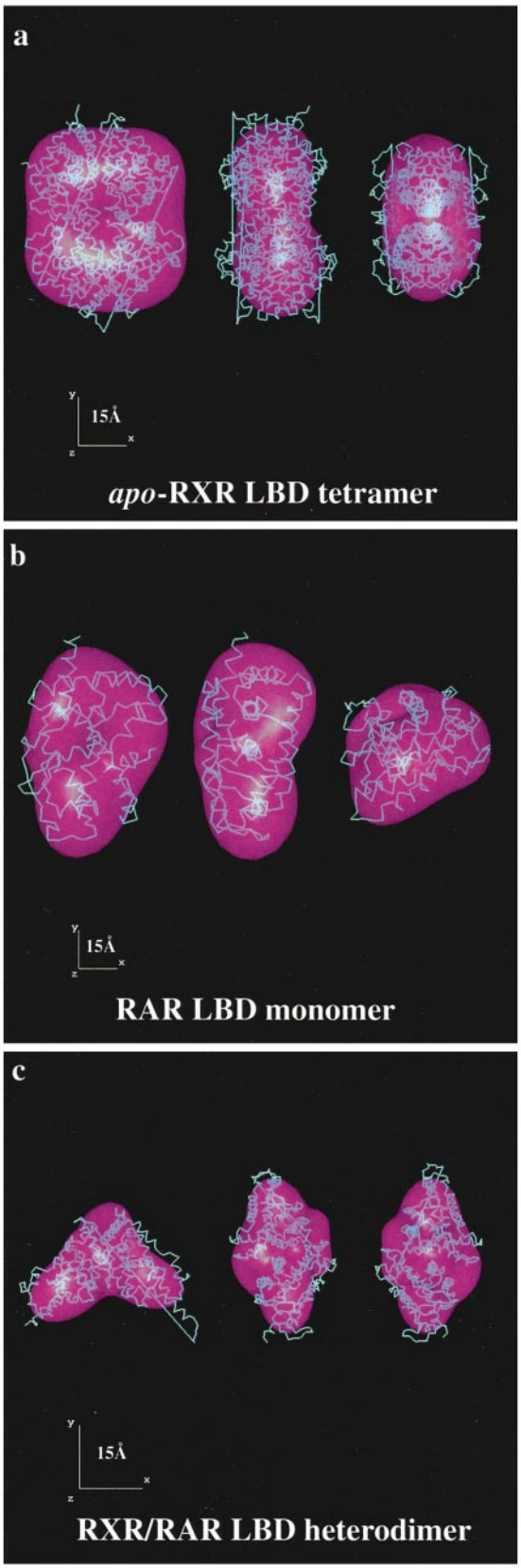

Figure 8. *Ab initio* 3D shape restoration retrieval attempts by simulated annealing minimization of dummy atom model with *DAMMIN*. Protein envelopes are described using spherical harmonics expansion (limited to $L = 5$) in the same way as used to calculate the scattering patterns in *CRYSOL* and *CRYSON* and are rendered using *ASSA*.[64] Retrieved particles rendered as transparent envelopes (magenta) are shown with the corresponding crystallographic structures (cyan) after optimal superimposition along the inertia axes using the program *SUPCOMB*. Scale bars are indicated. (a) *Apo*-RXRα LBD tetramer reconstruction (from SAXS data, final $\chi = 1.848$ at the end of minimization). (b) *Holo*-RARα LBD monomer reconstruction (from SANS data, final $\chi = 1.976$ at the end of minimization). (c) *Apo/apo*-RXRα/RARα LBD heterodimer reconstruction (from SAXS data, final $\chi = 1.406$ at the end of minimization).

available for interdimer stabilizing interactions whereas it is buried and in contact with the ligand 9-*cis*RA in the *holo*-form. Indeed we and others do observe that the binding of 9-*cis*RA induces dissociation of tetramers towards homodimers. The extreme stability of this tetramer might be the result of two cooperative mechanisms: (i) H12/protein core exchange; and (ii) dimer/dimer hydrophobic interface association. Furthermore, site-directed mutagenesis carried out on polar residues involved in ionic interactions stabilizing the tetrameric arrangement at the level of the interface also supports this model.

Ab initio low resolution three-dimensional shape reconstruction of retinoic acid receptor ligand binding domains

We investigated the low resolution structure of some of the molecular species using the *ab initio* simulated annealing procedure implemented in the program *DAMMIN*[27] (Materials and Methods). We used this complementary approach to assess independently the global solution structures of retinoid receptor LBDs. Several three-dimensional shape calculations were performed on *apo*-RXRα LBD tetramer, *holo*-RARα LBD monomer, *apo/apo* RXRα/RARα LBD heterodimer and *holo*-RXRα LBD homodimer (Figure 8). In the case of RXRα LBD *apo*-tetramer (Figure 8(a)), for which no structural crystallographic information was available when we performed this solution study, the *ab initio* reconstructed particle obtained is remarkably close to that obtained by a systematic, molecular modelling procedure. In particular, the reconstructed shape shows that the elongated model of two intertwined homodimers along the 2-fold symmetry axis is clearly favoured rather than a shorter and more compact and isometric model based on parallel or antiparallel packed homodimers. Note that *ab initio* shape reconstruction retrieved quite faithfully the overall discoidal and flat shape of the *apo*-RXRα LBD tetramer as it is seen in the crystal structure.

For RARα LBD monomer (Figure 8(b)) and for RXRα/RARα LBD heterodimer (Figures 8(c)), the *ab initio* reconstructed shapes were close to the crystallographically derived envelopes. In particular the reconstructed shapes of the RXRα/RARα

LBD heterodimer and of the RXRα LBD homodimer (data not shown) are in good agreement with the dimeric association mode and clearly show the characteristic bilobed shape of dimers, and validate both the relative orientation of subunits and geometry of dimeric arrangements of NR LBDs. Note that no symmetry constraints were imposed during *ab initio* envelope calculations with *DAMMIN*.

Conclusion and Perspectives

RXR the ubiquitous heterodimerization partner of both ligand-activated NRs and orphan receptors occupies a central position in NR signalling. The present solution study shows unambiguously the homodimeric structure of RXRα LBD liganded to its natural agonist 9-*cis* retinoic acid. Although the biological relevance of RXRα homodimers is still under discussion, almost all available structural data confirm their existence. The structural conservation of dimerization interfaces among NRs has been analysed[24,25] and the smaller interface observed in homo- or hetero-dimers involving RXR compared to those of ER and PPAR was tentatively associated with a weaker association that could be related to the ubiquitous character of RXR; differential stability of homo *versus* hetero dimeric association modes could account for the switch between the multiple NR partners available for RXR. Whether the observed tetramers have any biological relevance also remains to be elucidated. Despite their low resolution, solution data can complement high resolution structural crystallographic data. The present study underlines the peculiar and complex solution behaviour of RXR and emphasizes the crucial role of ligands in the subtle regulation of homodimeric *versus* heterodimeric association states of RXR in the NR signalling pathways.

Solution studies of the RXRα/RARα heterodimer, the functional entity *in vivo*, allowed us to highlight its structural stability and demonstrated a general agreement between the solution conformation and the model derived from crystal structures whatever the liganded state. Our SANS data showed that specific ligand binding induces a global compaction of the heterodimer assembly ($\Delta R_G = 1.5$-1.8 Å). Preliminary solution studies performed on VDR LBD and RXRα/VDR LBD heterodimers using the same combination of AUC and SAS techniques[48] have revealed similar solution properties for VDR when compared to RAR. Using SANS, we showed that the exclusively monomeric RARα LBD undergoes a conformational change ($\Delta R_G = 0.8$ Å) towards a more compact shape upon specific ligand binding; the observed conformations and rearrangements are in agreement with the mechanism inferred from crystal structures.

The only structural information (from X-ray crystallography and NMR spectroscopy) available for NRs to date concerns the isolated functional and structural domain DBDs and LBDs. No structural information, not even at low resolution, is available either for the full-length receptors or for the receptor/coregulator or receptor/corepressor complexes. Further structural characterization of the retinoid receptors RXR and RAR will imply the crystallization of the full-length receptors complexed to DNA harbouring their cognate target sequences. Solution small-angle scattering low resolution studies of RXR homodimers and RXR/RAR heterodimer complexes with cognate DNA might give precious information concerning the overall shape and size of such complexes, while the combination of SAS and of the available crystal structures might allow us to determine the relative orientation and position of the various domains building up these transcriptional factors.

Materials and Methods

Biochemistry sample preparation

Expression of human LBDs (wtRXRα, mtRXRα and wtRAR LBDs)

For isolated LBDs, each LBD was expressed in *Escherichia coli* BL21(DE3) cells harbouring a pET15b plasmid encoding for a N-terminal hexa-histidine tagged-LBD fusion protein; RXRα and RARα LBDs encompass residues Thr223 to Thr462 and Glu176 to Asp421, respectively. Freshly transformed cells were grown in 2 × LB-ampicillin medium at 37 °C until $A_{600\ nm}$ reached 0.6-0.8 and were then allowed to grow for another four to five hours at 25 °C after induction with 0.8 mM IPTG (isopropyl β thiogalactoside). For heterodimers, RXRα LBD was expressed in *E. coli* BL21(DE3) plysS cells harbouring a pET3a plasmid encoding for a ligand binding domain without the N-terminal hexa-histidine tag. Freshly transformed cells were grown in 2 × LB-ampicillin/chloramphenicol medium as described above. Cells were harvested by centrifugation, washed and then lysed by sonication.

Purification of isolated LBDs

Isolated LBDs were purified in three chromatographic steps. Proteins were first purified by metal chelating affinity chromatography on a cobalt-chelating column (Talon Clontech) with elution by imidazole steps. Protein fractions were then chromatographed on a Superdex S75-HR 26/60 gel filtration (Pharmacia). At this stage of the purification each protein behaved differently. Following the first step proteins were reconcentrated on Microcon-30 devices (Amicon-Grace) and treated with plasma bovine thrombin (1 unit per mg of protein at 4 °C during 48 hours in presence of 5 mM $CaCl_2$) in order to remove the hexa-histidine tag. To inactivate efficiently thrombin, Pefabloc (Boehringer-Manheim) was added to the concentrated protein pools at a final concentration of 5 mM. The last gel filtration chromatographic step was performed on an analytical Superdex S200-HR 10/30 (Pharmacia).

Purification of LBD heterodimers

Heterodimers of LBDs were also purified in three chromatographic steps. In order to ensure a perfect

RXR/RAR stoichiometry, heterodimers were obtained by copurification between N-terminal tagged RARα LBD and untagged RXRα LBD. An excess of tagged RARα LBD was used which could easily be removed from the heterodimer by gel filtration. Proteins were first purified by metal chelating affinity chromatography on a cobalt-chelating column using imidazole steps. After concentration on Centriprep-30 devices, protein fractions were then chromatographed on a Superdex S75-HR 26/60 gel filtration. Proteins were then reconcentrated on Microcon-30 devices, treated with bovine thrombin and finally gel filtrated as described above.

Hormone saturation of protein preparations

For purification made in the presence of the hormones 9-*cis*RA or all-*trans*RA, hormones were added to the crude extracts during lysis as a saturated ethanol solution (0.5% of the total sample volume) and allowed to incubate for one hour at 4 °C prior to the first affinity chromatographic step. This did not cause any detectable aggregation and was enough to saturate all receptor sites. Hormone was also added after the affinity chromatography step and in the elution buffers at 1 μM in the first gel filtration. All these purification steps and subsequent scattering measurements were performed under dimmed light to avoid photolysis of the photosensitive ligands.

Quality control of proteins

Protein purity was assessed using overloaded SDS-PAGE gels with Coomassie blue staining. Protein integrity was characterized by native-PAGE with Coomassie blue staining (Figure 2). In addition, the stoichiometry of the heterodimers was also observed by electro-spray mass spectrometry under non-denaturing conditions, which underlines the stability of the isolated species. Protein concentrations were determined spectrophotometrically from molar extinction coefficients at $\lambda = 280$ nm calculated from the amino acid compositions ($\varepsilon_{RAR} = 0.41$ with $M_r = 27{,}200$ Da and $\varepsilon_{RXR} = 0.58$ with $M_r = 28{,}400$ Da) and by the Bradford assay using bovine serum albumin as standard. The presence of the hormones was checked using their characteristic maximum absorption wavelength ($\lambda_{max}^{9\text{-cisRA}} = 343$ nm and $\lambda_{max}^{\text{all-transRA}} = 351$ nm). In each case, to avoid aggregation problems, only the top of the elution peak of the final gel filtration was used, without any further concentration step, in scattering measurements for Guinier analysis. Proteins were only reconcentrated for recording the weak intensities at high Q values, for which the monodispersity requirement is less stringent.

Analytical gel filtration

Analytical gel filtration experiments were performed on purified species concentrated on Centricon-30 devices by using a Superdex 200 pg HR 10/30 column (Pharmacia) at 4 °C with a flow rate of 0.5 ml min^{-1} and an injection volume of 0.5 ml. The chromatography buffer was 10 mM Tris (pH 8.0), 500 mM NaCl and 1 mM EDTA. Globular proteins with known hydrodynamic radii R_h were used as molecular weight standards to calibrate the column: bovine serum albumin ($M_r = 67{,}000$ Da, $R_h = 35.5$ Å), ovalbumin ($M_r = 43{,}000$ Da, $R_h = 30.5$ Å), chymotrypsinogen ($M_r = 25{,}000$ Da, $R_h = 20.9$ Å) and RNase ($M_r = 13{,}700$ Da, $R_h = 16.4$ Å). Molecular mass calculations and hydrodynamic Stokes radii were determined form plots of $-\log K_{av}$ *versus* M_r and $\sqrt[2]{-\log K_{av}}$ *versus* R_h respectively, with:

$$K_{av} = \frac{V_r - V_e}{V_t - V_e}$$

where V_r is the retention volume of the protein, V_e is the void or exclusion volume of the column (here $V_e = 8.0$ ml) and V_t is the total efficient volume of the column (here $V_t = 28.0$ ml).

Analytical ultracentrifugation and hydrodynamic modelling

Analytical ultracentrifugation

The experimental buffer (gel filtration) was 20 mM Tris (pH 8.0), 250 mM KCl and 1 mM EDTA. Sedimentation velocity and sedimentation equilibrium experiments were performed at a temperature of 20.1 °C using a Beckman Optima XL-A analytical ultracentrifuge (Beckman Instruments Inc. Palo Alto, CA) with absorbance monitoring. Protein concentrations were in the range of 0.5 to 1.8 mg/ml, corresponding to molar concentrations of 5 to 70 μM.

Sedimentation velocity

For sedimentation velocity experiments, samples were spun at 50,000 rpm and 55,000 rpm, respectively, for RARα and RXRα or RXRα/RARα samples. Consecutive scans were automatically recorded at regular intervals. The net sedimentation behaviour of macromolecules in a centrifugal field is described by the Svedberg equation.[29,30] The experimental sedimentation coefficients s were determined from the inflection points using the classical equation describing the motion of a solvent-solution boundary. Practically they were determined by the classical midpoint and the second moment point methods.[29,30] A third method was also used to determine the apparent sedimentation coefficients at the boundary using their distribution $g(s^*)$ calculated using the time derivative analysis method.[31,49] The experimental $g(s^*)$ profiles were fitted with a normal Gaussian distribution. This allowed different experimental determination of sedimentation coefficients.

Equilibrium sedimentation

For sedimentation equilibrium experiments, samples were spun at 12,000 rpm and systems were first allowed to equilibrate for 12 hours before absorbance profiles were compared at different times to ensure that system had reached equilibrium. Using non-linear least-squares analysis, these data sets were fitted using single component model and several equilibrium models including monomer/dimer, monomer/dimer/tetramer and dimer/tetramer.

Modelling of hydrodynamic properties

The hydrodynamic properties of macromolecules in solution were modelled with the program *HYDRO*[50] using hydrodynamic bead models based on crystallographic structures generated by the program *AtoB*[51] that uses the sequence and the tabulated specific volume of amino acid constituents. *HYDRO* allows the calculation of sedimentation and translational and rotational diffu-

sion coefficients of macromolecules of arbitrary shape. For an accurate description of the hydrodynamic properties of the molecules the number of beads was set as high as possible taking into account the supermatrix inversion calculation done in *HYDRO*.

Small angle scattering

SANS measurements and data processing

The experimental buffer (gel filtration) was 10 mM Tris (pH 8.0), 500 mM NaCl, 1 mM EDTA, 14 mM β-mercaptoethanol, 0.1 mM DIFP, 1 mM Chaps and 0.05 mM $C_{12}M$. Measurements were made in 100% H_2O buffers and 100% ^2H_2O buffers. SANS data were recorded at 4.8 °C at different concentrations of LBDs in H_2O and ^2H_2O buffers on the SANS instrument D11[52,53] at the high neutron flux reactor at ILL (Grenoble, France). Sample solutions were contained in quartz cells (Hellma, France) with a path length of 1 mm for H_2O measurements and 2 mm for ^2H_2O measurements. The cold neutron beam was monochromated using a helical slot velocity selector producing a wavelength spread $\Delta\lambda/\lambda$ of 9% (FWHM) at any incident wavelength λ. Smallest angle measurements were made at a sample-to-detector distance of 2.5 m with a collimation of 2.5 m and $\lambda = 10$ Å. This gives a useful Q-range of 0.015 $Å^{-1}$ to 0.092 $Å^{-1}$. Higher angle data were measured with a sample-detector distance of 1.2 m and a wavelength of 6 Å, giving a Q-range of 0.05 Å to 0.3 Å. The two-dimensional detector is a multi-wire chamber filled with BF_3, the size of detector is 64 cm × 64 cm^2 with 1 cm^2 spatial resolution.[52,53] The data were corrected for transmission, buffer and cell scattering and detector response function before being radially averaged to yield scattering curves of *I(Q)*. Guinier analyses and molecular mass calculations were performed on these fully processed data. All primary data reduction and Guinier analyses were carried out using standard ILL software (RNILS, XPOLLY, RGUIM and RPLOT).[54] In order to obtain sufficient statistical precision and to correct for the high incoherent scattering background of the H_2O solvent, extensive counting was performed on each sample and buffers. Typically each sample or buffer was sequentially counted three to five times one hour and, prior to global summation of all equivalent runs and correction for the solvent background, each measurement was processed independently to check for the absence of aggregation of the sample during data collection. Data in H_2O buffers could only be reliably measured in the lowest angle range (0.015 $Å^{-1}$ to 0.092 $Å^{-1}$). The average counting time in ^2H_2O buffer was only 30 minutes due to the much better signal-to-noise ratio arising from the low background of ^2H_2O buffers. As these data had a much greater statistical accuracy it was possible to measure them over the complete Q-range of 0.015 to 0.3 $Å^{-1}$ covered by the two different instrumental configurations.

SAXS measurements and data processing

The experimental buffer (gel filtration) was 10 mM Tris (pH 8.0), 250 mM NaCl, 1 mM EDTA, 10 mM DTT, 0.1 mM DIFP, 1 mM Chaps and 0.05 mM $C_{12}M$. DTT, an efficient radical scavenger, was added to minimise radiation damage. SAXS data were recorded on the SAXS instrument D24[55] at the synchrotron facility LURE-DCI (Orsay, France). The data acquisition system has been described.[56] The wavelength of the X-rays was $\lambda = 1.488$ Å (K-edge of Ni) and the sample-to-detector distance was 1582 mm yielding a Q increment per channel of $\Delta Q = 0{,}0012$ $Å.^{-1}$ $channel^{-1}$. The linear position-sensitive detector is a 512 channel gas chamber filled with a two-bar mixture of Xe_2/C_2H_6 (90%/10%). The effective Q-range extended from 0.01 $Å^{-1}$ to 0.3 $Å^{-1}$. For the small-angle analysis, data were analysed in the Q region extending from 0.01 $Å^{-1}$ to 0.08 $Å^{-1}$. 70 µl of sample were injected into a quartz capillary under vacuum[57] kept at a constant temperature of 5 °C and were recovered after the measurement. Nine or 18 frames of 200 seconds each were recorded depending on the sample concentration. Frames were visually inspected to check for X-ray damage; none was found. All data were scaled to the transmitted intensity, before computing the average and standard deviation of each measurement and subtracting the scattering from the corresponding buffer.

SAS data analysis

Guinier analysis

The data in the lowest angle range when plotted as $\ln I(Q)$ *versus* Q^2 give the R_G value and $I(0)$ the forward scattering intensity extrapolated at zero angle[58] with:

$$\ln I(Q) = \ln I(0) - \frac{Q^2}{3} R_G^2 \quad \text{with} \quad Q = \frac{4\pi \sin\theta}{\lambda}$$

where Q is the scattering vector for a scattering angle of 2θ and a wavelength of λ. For a sphere, this expression is valid in a QR_G range up to 1.3 which can be extended up to 2.0 in some cases, the most conservative limit being in the range of $QR_G = 1$. The value of $I(0)$ allows calculation of an apparent molecular mass M_r of the particle in solution as far as the concentration c of the sample has been determined accurately.[59]

Distance distribution function *P(r)*

Indirect transformation of the scattering data $I(Q)$ in the reciprocal space into that in real space $P(r)$ were carried out using the *ITP*[60] and *GNOM*[61,62] programs for SANS data and *GNOM* program for SAXS data. Calculations by either of the two programs include an estimate of the D_{max}. As $P(r)$ corresponds to the distribution of distances r between any two volume elements within one particle, it offers an alternative calculation of $I(0)$ its zeroth moment, R_G its second moment and gives also the chord D_{max} the maximum dimension of the macromolecule:

$$P(r) = \frac{1}{2\pi^2} \int_0^\infty I(Q) \cdot r \cdot \sin(Q \cdot r) dQ$$

and

$$R_G^2 = \frac{r^2 P(r) dr}{2P(r) dr}$$

D_{max} was determined from the value of r when $P(r)$ became zero at larger r values; a range of maximum chords D_{max} was systematically tested for integration and the final choice of D_{max} was based on four essential criteria:(*i*) the restriction $P(r = 0) = 0$ (this constraint was first released for the first estimation of $P(r)$ and was then applied for the final estimation); (*ii*) $P(r)$ should exhibit

positive values; (*iii*) the R_G from *GNOM* or *ITP* should agree with the R_G from Guinier analysis; and (*iv*) the $P(r)$ curve should be stable as D_{max} is increased beyond the estimated macromolecular length. Geometrical corrections were performed for experimental curves only in the case of neutrons data.

Scattering curve calculation and fitting

The scattering intensity $I(Q)$ from particles in a solvent with scattering length density ρ_0 can be evaluated as:

$$I(Q) = \langle |A_a(\vec{Q}) - \rho_0 A_e(\vec{Q}) + \delta\rho A_{hs}(\vec{Q})|^2 \rangle_\Omega \text{ with } Q = (Q, \Omega)$$

The particle has a scattering density ρ_a and is surrounded by a solvent with an average scattering density ρ_o; the hydration shell is depicted by a border layer of effective thickness Δ and density ρ_b different from ρ_0. Here $A_a(Q)$, $A_e(Q)$ and $A_{hs}(Q)$ are the amplitudes from the particle *in vacuo*, the excluded volume and the hydration shell, respectively. Ω is the solid angle in reciprocal space. $I(Q)$ is an average over all orientations particles in solution. The particle shape is described by an angular envelope function. The scattering from the hydration shell is simulated by surrounding the envelope function with a layer of thickness $\Delta = 3$ Å and density ρ_b. Experimental scattering curves $I_{exp}(Q)$ are fitted against calculated scattering curves $I_{calc}(Q)$ using two parameters, the total excluded volume V and the contrast of the border layer $\delta\rho = \rho_b\text{-}\rho_o$ to minimize the discrepancy χ defined as:

$$\chi^2 = \frac{1}{N-1}\sum_{i=1}^{N}\left(\frac{I_{exp}(Q_i) - I_{calc}(Q_i)}{\sigma(Q_i)}\right)^2$$

where N is the number of experimental points and $\sigma(Q_i)$ the associated standard deviations. In practice, theoretical scattering curves and R_G were calculated using *CRYSOL*[26] and *CRYSON*[36] programs and automatically fitted against experimental curves. In the case of neutron data, a 100 % ^2H_2O content of buffer and 10 % rate of non-exchanged labile hydrogen atoms were assumed. Smearing corrections were performed for experimental curves only in the case of neutrons data. The resulting fitting parameters adjusted in *CRYSOL* and *CRYSON* corresponded to a reasonable description of the hydration properties of the particles in solution.

Receptor modelling

Crystallographic structures of LBDs were used to generate all the models used in calculations. At the time of this study five structures of retinoic acid receptor LBDs were available: the *apo*-homodimer of wtRXRα LBD (PDB entry: *1LBD*), the *holo*-monomer wtRXRα LBD (PDB entry: *1FBY*) bound to 9-*cis*RA, the *holo* wtRARα LBDs complexed to either all-*trans*RA (PDB entry *2LBD*) and 9-*cis*RA and a heterodimer wtRARα/mutRXRα (PDB entry: *1DKF*). The *apo*-wtRARα LBD model was generated using the crystallographic model of wtRXRα *apo*-LBD as a template for modelling using *MODELLER*. Using the crystallographic structure of the heterodimer and assuming the same dimerization interface several heterodimer models were then generated: *apo/apo*, *apo/holo* and *holo/holo* wtRXRα/wtRARα. A *holo*-homodimer of RXRα LBD was also generated assuming the same dimerization interface as this observed in the *apo*-RXRα LBD homodimer structure. The coordinates of *apo*-RXRα LBD tetramer were kindly provided by Dr E. Xu.

Ab initio three-dimensional reconstruction of molecular shapes

Low-resolution model retrieving from one-dimensional small angle X-ray scattering data in solution was performed using the program *DAMMIN*.[27] A DAM (Dummy Atom Model) is randomly generated and is composed of an array of given contrast spheres densely packed on a hexagonal face-centred cubic lattice with a given lattice constant. The scattering intensity from a given DAM is calculated by global summation over all dummy atoms using spherical harmonics expansion to represent partial amplitudes. *Ab initio* reconstruction consists in finding a DAM configuration corresponding to a minimal value of a goal energy function and minimizing the discrepancy between experimental and DAM calculated scattering curves. Compactness, connectivity and looseness of the DAM are described by functions that are taken into account during this global minimization procedure that uses simulated annealing. The algorithm proceeds iteratively through a single dummy atom move. SAXS and SANS profiles were subjected to several independent reconstructions runs.

Acknowledgements

We are extremely grateful to Drs D.I. Svergun and M. Kozin for kindly providing us the program *SUPCOMB*. We thank Dr E. Xu for kindly providing us the coordinates of *apo*-RXRα LBD tetramer before their deposition at the Protein Data Bank. We are indebted to Dr B. Rees for successful suggestions during modelling of *apo*-RXR tetramer. We are also grateful to Dr M. Delarue for helpful discussions. We thank Dr J.-M. Wurtz for receptor modelling. We thank Dr J.-P. Samama for allowing us to benefit from the analytical ultracentrifugation ressources. We thank the technical staffs of LURE and ILL for technical support on the beam lines. This work was supported by funds from Bristol-Myers-Squibb, the INSERM, the CNRS and grants from the Ministère de la Recherche et de l'Enseignement Supérieur, the Fondation pour la Recherche Médicale and the Association pour la Recherche sur le Cancer (P.F.E.).

References

1. Gronemeyer, H. & Laudet, V. (1995). In *Protein profile: Transcription Factors 3: Nuclear Receptors*, vol. 2-11, pp. 1173-1226, Academic Press, New York.
2. Heyman, R. A., Mangelsdorf, D. J., Dyck, J. A., Eichele, G., Evans, R. M. & Thaller, C. (1992). 9-*cis* retinoic acid is a high affinity ligand for the retinoid X receptor. *Cell,* **68**, 397-406.
3. Levin, A. A., Sturzenbecker, L. J., Kazmer, S., Bosakowski, T., Huselton, C. & Allenby, G., *et al.* (1992). 9-*cis* retinoic acid stereoisomer binds and activates the nuclear receptor RXRα. *Nature,* **355**, 359-361.
4. Mangelsdorf, D. J., Umesono, K. & Evans, R. M. (1994). The retinoid receptors. In *The Retinoids. Biology, Chemistry and Medicine*, chapt. 8, pp. 319-349, Raven Press Ltd.

5. Mangelsdorf, D. J., Thummel, C., Beato, M., Herrlich, P., Schütz, G. & Umesono, K., *et al*. (1995). The nuclear receptor superfamily: the second decade. *Cell,* **83**, 835-839.
6. Mangelsdorf, D. J. & Evans, R. M. (1995). The RXR heterodimers and orphan receptors. *Cell,* **83**, 841-850.
7. Chambon, P. (1996). A decade of molecular biology of retinoic acid receptors. *FASEB J.* **10**, 940-954.
8. Minucci, S., Leid, M., Toyama, R., Saint-Jeannet, J-P. & Peterson, V. J., *et al*. (1997). Retinoid X receptor RXR within the RXR retinoic acid receptor heterodimer binds its ligand and enhances retinoid dependent gene expression. *Mol. Cell. Biol.* **17**, 644-655.
9. Botling, J., Castro, D. S., Oberg, F., Nilsson, K. & Perlmann, T. (1997). Retinoic acid receptor/retinoid X receptor heterodimers can be activated through both subunits providing a basis for synergistic transactivation and cellular differentiation. *J. Mol. Biol.* **272**, 9444-9449.
10. Dilworth, D. J., Fromental-Ramain, C., Remboutsika, E., Benecke, A. & Chambon, P. (1999). Ligand dependent activation of transcription in vitro by retinoic acid receptor α/retinoid X receptor α heterodimers that mimics transactivation by retinoids *in vivo*. *Proc. Natl Acad. Sci., USA,* **96**, 1995-2000.
11. Bourguet, W., Ruff, M., Chambon, P., Gronemeyer, H. & Moras, D. (1995). Crystal structure of the ligand binding domain of the human nuclear receptor RXRα. *Nature,* **375**, 377-382.
12. Egea, P. F., Mitschler, A., Rochel, N., Ruff, M., Chambon, P. & Moras, D. (2000). Crystal structure of the human RXRα ligand-binding domain bound to its natural ligand: 9-*cis* retinoic acid. *EMBO,* **19**, 2592-2601.
13. Renaud, J.-P., Rochel, N., Ruff, M., Vivat, V., Chambon, P., Gronemeyer, H. & Moras, D. (1995). Crystal structure of the RARγ ligand binding domain bound to all-*trans* retinoic acid. *Nature,* **378**, 681-689.
14. Klaholz, B. P., Renaud, J. P., Mitschler, A., Zusi, C., Chambon, P., Gronemeyer, H. & Moras, D. (1998). Conformational adaptation of agonists to the human nuclear receptor RARγ. *Nature Struct. Biol.* **5**, 199-202.
15. Wagner, R. L., Apriletti, J. W., McGrawth, M. E., West, B. L., Baxter, J. D. & Fletterick, R. J. (1995). A structural role for hormone in the thyroid hormone receptor. *Nature,* **378**, 690-697.
16. Xu, H. E., Lambert, M. H., Montana, V. G., Parks, D. J., Blanchard, S. G., Brown, P. J., Sternbach, D. D., Lehman, J. M., Wisely, T. M., Kliewer, S. A. & Milburn, M. V. (1999). Molecular recognition of fatty acids by peroxysome proliferator-actuated receptors. *Mol. Cell,* **3**, 397-403.
17. Brzozowski, A. M., Pike, A. C. W., Dauter, Z., Hubbard, R. E., Bonn, T. & Engström, O. *et al*. (1997). Molecular basis of agonism and antagonism in the oestrogen receptor. *Nature,* **389**, 753-758.
18. Williams, S. P. & Sigler, P. B. (1998). Atomic structure of progesterone complexed with its receptor. *Nature,* **393**, 392-396.
19. Tanenbaum, D. M., Wang, Y., Williams, S. P. & Sigler, P. B. (1998). Crystallographic comparison of the estrogen and progesterone receptor's ligand binding domain. *Proc. Natl Acad. Sci. USA,* **95**, 5998-6003.
20. Rochel, N., Wurtz, J.-M., Mitschler, A., Klaholz, B. & Moras, D. (2000). Crystal structure of the nuclear receptor for vitamin D bound to its natural ligand. *Mol. Cell,* **5**, 173-179.
21. Wurtz, J-M., Bourguet, W., Renaud, J.-P., Vivat, V., Chambon, P., Moras, D. & Gronemeyer, H. (1996). A canonical structure for the ligand binding domains of nuclear receptors. *Nature Struct. Biol.* **3**, 87-94.
22. Moras, D. & Gronemeyer, H. (1998). The nuclear receptor ligand binding domain: structure and function. *Curr. Opin. Cell Biol.* **10**, 384-391.
23. Egea, P. F., Klaholz, B. P. & Moras, D. (2000). Ligand-protein interactions in nuclear receptors of hormones. *FEBS Letters,* **476**, 62-67.
24. Bourguet, W., Vivat, V., Wurtz, J-M., Chambon, P., Gronemeyer, H. & Moras, D. (2000). Crystal structure of a heterodimeric complex of RAR and RXR ligand-binding domain. *Mol. Cell,* **5**, 289-298.
25. Gampe, R. T., Montana, V. G., Lambert, M. H., Miller, A. B., Bledsoe, R. K. & Milburn, M. V. *et al.* (2000). Asymmetry in the PPARγ/RXRα crystal reveals the molecular basis of heterodimerization among nuclear receptors. *Mol. Cell.* **5**, 545-555.
26. Svergun, D. I., Barberato, C. & Koch, M. H. J. (1995). *CRYSOL* a program to evaluate X-ray solution scattering of biological macromolecules form atomic coordinates. *J. Appl. Crystallog.* **28**, 768-773.
27. Svergun, D. I. (1999). Restoring low resolution structure of biological macromolecules from solution scattering using simulated annealing. *Biophys. J.* **76**, 2879-2886.
28. Byron, O. & Gilbert, R. J. C. (2000). Neutron scattering: good news for biotechnology. *Curr. Opin. Biotechnol.* **11**, 72-80.
29. Hansen, J. C., Lebowitz, J. & Demeler, B. (1994). Analytical ultracentrifugation of complex macromolecular systems. *Biochemistry,* **33**, 13155-13163.
30. Hensley, P. (1996). Defining the structure and stability of macromolecular assemblies in solution: the re-emergence of analytical ultracentrifugation as a practical tool. *Structure,* **4**, 367-373.
31. Stafford, W. F. (1997). Sedimentation velocity spins a new weave for an old fabric. *Curr. Opin. Biotechnol.* **8**, 14-24.
32. Kersten, S., Pan, L. & Noy, N. (1995). On the role of ligand in retinoid signalling:positive cooperativity in the interactions of 9-cis retinoic acid with tetramers of the retinoic acid receptors. *Biochemistry,* **34**, 14263-14269.
33. Kersten, S., Pan, L., Chambon, P., Gronenmeyer, H. & Noy, N. (1995). Role of ligand in retinoid signalling. 9-*cis* retinoic acid modulates the oligomeric state of the retinoid. *Biochemistry,* **34**, 13717-13721.
34. Kersten, S., Kelleher, D., Chambon, P., Gronemeyer, H. & Noy, N. (1995). Retinoid X receptor forms tetramers in solution. *Proc. Natl Acad. Sci. USA,* **92**, 8645-8649.
35. Stuhrmann, H. B. & Fuess, H. A. (1976). Neutron small-angle scattering study of hen egg-white lysozyme. *Acta Crystallog. sect. A,* **32**, 67-74.
36. Svergun, D. I., Richard, S., Koch, M. H. J., Sayers, Z., Kuprin, S. & Zaccai, G. (1998). Protein hydration in solution: experimental observation by X-rays and neutron scattering. *Proc. Natl Acad. Sci. USA,* **95**, 2267-2272.
37. Johnson, B. A., Wilson, E. M., Li, Y., Moller, D. E., Smith, R. G. & Zhou, G. (2000). Ligand induced stabilization of PPARγ monitored by NMR spectroscopy: implications for nuclear receptors activation. *J. Mol. Biol.* **298**, 187-194.

38. Allenby, G., Bocquel, M. T., Saunders, M., Kazmer, M., Speck, J. & Rosenberger, M. *et al*. (1993). Retinoic acid receptors and retinoid X receptors: interactions with endogenous retinoic acid. *Proc. Natl Acad. Sci. USA,* **90**, 30-34.
39. Allegretto, E. A., McClurg, M. R., Lazarchik, S. B., Clemm, D. L., Kerner, S. A. & Elgort, M. G., *et al.* (1993). Transactivation properties of retinoic acid and retinoid X receptor in mammalian cells and yeast. *J. Biol. Chem.* **268**, 26625-26633.
40. Kersten, S., Dawson, M. I., Lewis, B. A. & Noy, N. (1996). Individual subunits of heterodimers comprised of retinoic acid and retinoic X receptor with their target ligands independently. *Biochemistry,* **35**, 3816-3824.
41. Dong, D. & Noy, N. (1998). Heterodimer formation by retinoid X receptor: regulation by ligands and by the receptor's self association properties. *Biochemistry,* **37**, 10691-10700.
42. Kersten, S., Gronemeyer, H. & Noy, N. (1997). The DNA binding pattern of the retinoid X receptor is regulated by ligand dependent modulation of its oligomeric state. *J. Biol. Chem.* **272**, 12771-12777.
43. Kersten, S., Reczek, P. R. & Noy, N. (1997). The tetramerization region of the retinoid X receptor is important for transcriptional activation by the receptor. *J. Biol. Chem.* **272**, 29759-29768.
44. Chen, Z. P., Iyer, J., Bourguet, W., Held, P., Mioskowski, C. & Lebeau, L. *et al*. (1998). Ligand and DNA induced dissociation of RXR tetramers. *J. Mol. Biol.* **275**, 55-65.
45. Gampe, R. T., Montana, V. G., Lambert, M. H., Wisely, G. B., Milburn, M. V. & Xu, E. H. (2000). Structural basis for autorepression of retinoid X receptor by tetramer formation and the AF-2 helix. *Genes Dev.* **14**, 2229-2241.
46. Perkins, S. J., Ashton, A. W., Boehm, M. K. & Chamberlain, D. (1998). Molecular structures from low angle X-ray and neutron scattering. *Int. J. Macromol.* **22**, 1-16.
47. Zhang, J., Hu, X. & Lazar, M. A. (1999). A novel role for helix 12 of retinoid X receptor in regulating repression. *Mol. Cell. Biol.* **19**, 6448-6457.
48. Rochel, N., Tocchini-Valentini, G., Egea, P. F., Juntunen, K., Garnier, J.-M., Vihko, P. & Moras, D. (2001). Functional and structural characterization of the insertion region in the ligand-binding domain of the vitamin D nuclear receptor. *Eur. J. Biochem.,* **268**, in the press.
49. Stafford, W. F. (1992). Boundary analysis in sedimentation transport experiments: a procedure for obtaining sedimentation coefficient distributions using the time derivative of the concentration profile. *Anal. Biochem.* **203**, 295-301.
50. Garcia de la Torre, J., Navarro, S., Lopez Martinez, M. C., Diaz, F. G. & Lopez Cascales, J. J. (1994). *HYDRO*: a computer program for the prediction of hydrodynamic properties of macromolecules. *Biophys. J.* **67**, 530-531.
51. Byron, O. (1997). Construction of hydrodynamic bead models from high-resolution X-ray crystallographic or nuclear magnetic resonance data. *Biophys. J.* **72**, 361-372.
52. Ibel, K. (1976). The neutron small-angle camera D11 at the high flux reactor. Grenoble. *J. Appl. Crystallog.* **9**, 296-309.
53. Lindner, P., May, R. P. & Timmins, P. A. (1992). Upgrading of the SANS instrument D11 at the ILL. *Physica B.* **180**, 967-972.
54. Ghosh, R. E., Egelhaaf, S. U. & Rennie, A. R. (1998). *A Computing Guide for Small-Angle Scattering Experiments*, Institut Laue-Langevin, ILL98GH14T.
55. Depautex, C., Desvignes, P., Leboucher, P., Lemonnier, M., Dagenaux, D., Benoit, J. P. & Vachette, P. (1987). The small angle X-ray scattering instrument D24, CNRS Annual Report LURE75, Orsay, France.
56. Boulin, C., Kempf, R., Koch, M. H. J. & McLaughlin, S. M. (1986). Data appraisal, evaluation and display for synchrotron radiation experiments:hardware and software. *Nucl. Instr. Methods,* **A249**, 399-407.
57. Dubuisson, J. M., Decamps, T. & Vachette, P. (1997). Improved signal-to-background ratio in small angle X-ray scattering experiments with synchrotron radiation using an evacuated cell for solutions. *J. Appl. Crystallog.* **30**, 49-54.
58. Guinier, A. & Fournet, G. (1995). *Small Angle Scattering of X-rays*, John Wiley & Sons Inc., New York.
59. Jacrot, B. & Zaccai, G. (1981). Determination of molecular weight by neutron scattering. *Biopolymers,* **20**, 2413-2426.
60. Glatter, O. (1977). A new method for the evaluation of small-angle scattering data. *J. Appl. Crystallog.* **10**, 415-421.
61. Svergun, D. I. (1992). Determination of the regularization parameter in indirect transform methods using perceptual criteria. *J. Appl. Crystallog.* **25**, 495-503.
62. Svergun, D. I. (1993). A direct indirect method of small angle scattering data treatment. *J. Appl. Crystallog.* **26**, 258-267.
63. Philippsen, A. (1999). *DINO:* visualizing structural biology, On http//www. bioz. unibas. ch/~xray/dino.
64. Kozin, M. B., Volkov, V. V. & Svergun, D. I. (1997). *ASSA* - a program for three-dimensional rendering in solution scattering from biopolymers. *J. Appl. Crystallog.* **30**, 811-815.

Edited by M. F. Moody

(Received 19 July 2000; received in revised form 21 December 2000; accepted 27 December 2000)